

University of California - Davis

# Probing Models with Near Degeneracy of the Chargino and LSP at a Linear $e^+e^-$ Collider

John F. Gunion and Stephen Mrenna

*Davis Institute for High Energy Physics  
 University of California, Davis, CA 95616*

## Abstract

For some choices of soft SUSY-breaking parameters, the LSP is a stable neutralino  $\tilde{\chi}_1^0$ , the NLSP is a chargino  $\tilde{\chi}_1^\pm$  almost degenerate in mass with the LSP ( $\Delta m_{\tilde{\chi}} \equiv m_{\tilde{\chi}_1^\pm} - m_{\tilde{\chi}_1^0} \sim m_\pi$ -few GeV), and all other sparticles are relatively heavy. We discuss the potential of a  $\sqrt{s} \sim 600$  GeV  $e^+e^-$  collider for studying such models.

**1. Introduction.** As part of the process of planning for future HEP experimental facilities, it is important to evaluate as many motivated scenarios for new physics as possible. Certainly, supersymmetry ranks as one of the most successful models of physics beyond the Standard Model, since it can approximately reproduce Standard Model predictions at low energies, while explaining the hierarchy problem. However, the mechanism of supersymmetry breaking is not well understood. In general, the different sources of breaking – gravitational interactions, gauge interactions, the conformal anomaly, etc. – lead to different hierarchies of sparticle masses. Many sources may be present at once, so the true model may be quite complicated. Here, we explore a relatively well-motivated set of models in which the gaugino masses are non-universal at the GUT scale and, in particular, are such that there is a quite small mass splitting between the lightest chargino ( $\tilde{\chi}_1^\pm$ ) and the lightest neutralino ( $\tilde{\chi}_1^0$ ), which is the LSP. Small  $\Delta m_{\tilde{\chi}} \equiv m_{\tilde{\chi}_1^\pm} - m_{\tilde{\chi}_1^0}$  occurs when  $M_2 < M_1 \ll |\mu|$ , which arises naturally when the gaugino masses are dominated by or entirely generated by loop corrections. Models of this type include the O–II superstring model [1, 2, 3, 4] and the (AMSB) models in which SUSY-breaking arises entirely from the conformal anomaly [5, 6, 7]. The same hierarchy also occurs when SUSY is broken by an  $F$ -term that is not an SU(5) singlet but rather is a member of the **200** representation contained in  $(\mathbf{24} \times \mathbf{24})_{\text{symmetric}} = \mathbf{1} \oplus \mathbf{24} \oplus \mathbf{75} \oplus \mathbf{200}$  [8]. Techniques for detecting and studying supersymmetry are very dependent upon  $\Delta m_{\tilde{\chi}}$  and on the relative magnitude of  $m_{\tilde{\chi}_1^\pm} \sim m_{\tilde{\chi}_1^0}$  as compared to other supersymmetric particles. Previous discussions of small  $\Delta m_{\tilde{\chi}}$  scenarios at lepton colliders include early studies in the context of the O-II model [2, 3, 4] and various studies specific to the AMSB boundary conditions [9, 10, 11, 12]. This study will focus on signals and parameter determination for small  $\Delta m_{\tilde{\chi}}$  at a  $\sqrt{s} \sim 450 - 600$  GeV,  $L \sim 1$  ab $^{-1}$  linear  $e^+e^-$  collider (LC) when the only SUSY particles kinematically accessible at the LC are the  $\tilde{\chi}_1^0$  and  $\tilde{\chi}_1^\pm$ .

To illustrate the possibilities for  $\Delta m_{\tilde{\chi}}$  and other gaugino masses, it is useful to give some tree-level results for the gaugino mass parameters at the scale  $m_Z$ . The O–II model with  $\delta_{GS} = -4$  yields  $M_3$  :

$M_2 : M_1 = 6 : 10 : 10.6$ , the O–II model with  $\delta_{GS} = 0$  (equivalent to the simplest version of the conformal anomaly, AMSB, approach) yields  $M_3 : M_2 : M_1 = 3 : 0.3 : 1$ , while the **200** model yields  $6 : 4 : 10$ . As a result: in the **200** model and the O–II  $\delta_{GS} = 0$  (or pure AMSB) model,  $M_2 \ll M_1$  and  $\Delta m_{\tilde{\chi}} \equiv m_{\tilde{\chi}_1^\pm} - m_{\tilde{\chi}_1^0}$  can be smaller than  $\sim m_\pi$  at tree-level; in the O–II  $\delta_{GS} = -4$  case,  $M_2$  is only slightly less than  $M_1$  implying that  $\Delta m_{\tilde{\chi}} < \text{a few GeV}$  is very typical —  $\Delta m_{\tilde{\chi}} < 1 \text{ GeV}$  if  $|\mu| \gtrsim 1 \text{ TeV}$  as when RGE electroweak symmetry breaking is imposed [3]. Loop corrections can be significant. In particular, even if  $\Delta m_{\tilde{\chi}} < m_\pi$  at tree-level, radiative corrections [9, 13, 14] usually increase  $\Delta m_{\tilde{\chi}}$  to above  $m_\pi$  (see e.g. the  $\Delta m_{\tilde{\chi}}$  graphs in [3]);  $\Delta m_{\tilde{\chi}} < m_\pi$  is only possible for very special parameter choices. Most typically,  $\Delta m_{\tilde{\chi}}$  is predicted to lie in the range from slightly above  $m_\pi$  to several GeV.

All other SUSY particles could have masses substantially above  $m_{\tilde{\chi}_1^\pm}$ . In particular, in the O–II  $\delta_{GS} = 0$  and AMSB models,  $m_{\tilde{\chi}_2^0}$  is significantly larger than  $m_{\tilde{\chi}_1^\pm}$ . Only in the O–II  $\delta_{GS} = -4$  model is  $m_{\tilde{\chi}_2^0}$  close to  $m_{\tilde{\chi}_1^\pm}$ . In most cases, large  $|\mu|$  is required by radiative symmetry breaking so that the  $\tilde{\chi}_2^\pm$ ,  $\tilde{\chi}_3^0$  and  $\tilde{\chi}_4^0$  are very heavy. The masses for the squarks and sleptons are uncertain, but could be quite large, which is the case on which we focus. In particular, we neglect sneutrino exchange contributions to the  $\tilde{\chi}_1^+ \tilde{\chi}_1^-$  and  $\gamma \tilde{\chi}_1^+ \tilde{\chi}_1^-$  cross sections. For example, both cross sections start to become increasingly suppressed for  $\sqrt{s} \sim 600 \text{ GeV}$  as the electron sneutrino mass is decreased below 1 TeV; see, for example, [15].

The neutralino and chargino couplings to  $W$  and  $Z$  bosons in the wino-LSP scenario were reviewed in [11]. One finds that the  $Z \tilde{\chi}_1^0 \tilde{\chi}_1^0$ ,  $Z \tilde{\chi}_1^0 \tilde{\chi}_2^0$ ,  $Z \tilde{\chi}_2^0 \tilde{\chi}_2^0$ , and  $W^\mp \tilde{\chi}_1^\pm \tilde{\chi}_2^0$  couplings (and corresponding cross sections) are all small, while  $e^+ e^- \rightarrow Z, \gamma \rightarrow \tilde{\chi}_1^+ \tilde{\chi}_1^-$ ,  $\gamma \tilde{\chi}_1^+ \tilde{\chi}_1^-$  and  $e^+ e^- \rightarrow W^\mp \tilde{\chi}_1^\pm \tilde{\chi}_1^0$  can have large rates.

$\Delta m_{\tilde{\chi}}$ (MeV)	125	130	135	138	140	142.5	150
$c\tau$ (cm)	1155	918.4	754.1	671.5	317.2	23.97	10.89
$\Delta m_{\tilde{\chi}}$ (MeV)	160	180	185	200	250	300	500
$c\tau$ (cm)	6.865	3.719	3.291	2.381	1.042	0.5561	0.1023
$\Delta m_{\tilde{\chi}}$ (MeV)	600	700	800	900	1000	1500	2000
$c\tau$ (cm)	0.055	0.033	0.019	0.011	0.0072	0.0013	0.00036

Table 1: Summary of  $c\tau$  values as a function of  $\Delta m_{\tilde{\chi}}$ .

The most critical ingredients in the phenomenology of such models are the lifetime and the decay modes of the  $\tilde{\chi}_1^\pm$ , which in turn depend almost entirely on  $\Delta m_{\tilde{\chi}}$  when the latter is small. The  $c\tau$  and branching ratios of the  $\tilde{\chi}_1^\pm$  as a function of  $\Delta m_{\tilde{\chi}}$  have been computed in [4]. For  $\Delta m_{\tilde{\chi}} < m_\pi$ , only  $\tilde{\chi}_1^\pm \rightarrow e^\pm \nu_e \tilde{\chi}_1^0$  is important and  $c\tau > 10 \text{ m}$ . Once  $\Delta m_{\tilde{\chi}} > m_\pi$ , the  $\tilde{\chi}_1^\pm \rightarrow \pi^\pm \tilde{\chi}_1^0$  mode turns on and is dominant for  $\Delta m_{\tilde{\chi}} \lesssim 800 \text{ MeV}$ , at which point the multi-pion modes start to become important: correspondingly, one finds  $c\tau \lesssim 10 - 20 \text{ cm}$  for  $\Delta m_{\tilde{\chi}}$  just above  $m_\pi$  decreasing to  $c\tau < 100 \mu\text{m}$  by  $\Delta m_{\tilde{\chi}} \sim 1 \text{ GeV}$ . For later reference, we give some specific values of  $c\tau$  as a function of  $\Delta m_{\tilde{\chi}}$  in Table 1.

Finally, we wish to comment on what values for  $m_{\tilde{\chi}_1^\pm}$  are most natural in the context we are considering. The constraint from fine-tuning, though somewhat ill-defined, does provide some guidance. The degree of fine-tuning is largely controlled by the magnitude of the gluino mass. In the models discussed above there

are considerable differences in the ratio of  $M_3/M_2$ . This ratio is largest ( $\sim 9$ ) in the  $(\delta_{GS} = 0)/\text{AMSB}$  scenario and fine tuning increases rapidly [16] with  $M_2 \sim m_{\tilde{\chi}_1^\pm}$  to levels that are highly problematical once  $m_{\tilde{\chi}_1^\pm} > 200$  GeV. In the other scenarios  $M_3$  is close to  $M_2$  and fine-tuning is a less severe concern. The main focus of this paper will be on scenarios in which the chargino and neutralino are highly degenerate, which is most naturally the case in the  $(\delta_{GS} = 0)/\text{AMSB}$  scenario. Thus, our focus will be on procedures relevant for  $m_{\tilde{\chi}_1^\pm} \lesssim 200$  GeV and  $\Delta m_{\tilde{\chi}} < 1$  GeV.

**2. General Discussion of Detector and Signals.** For our discussions, we consider a detector with the components listed in Table 2. (See [11] for further details.) The SVX, CT and PS all give (independent) measurements of the  $dE/dx$  from ionization of a track passing through them. This makes it possible to distinguish a heavily-ionizing chargino (which would be  $\geq$  twice minimal ionizing [2MIP] for  $\beta\gamma \leq 0.85$ ) from an isolated minimally ionizing particle [1MIP]. The net discrimination factor would probably be of order  $\text{few} \times 10^{-5}$ . In our simulations, we employed an efficiency of 90% for tracks with  $\beta\gamma < 0.85$  [17].

The possible signals based upon detecting a non-promptly decaying  $\tilde{\chi}_1^\pm$  were detailed for a hadron collider in [11]. Appropriately modified versions for  $\tilde{\chi}_1^+ \tilde{\chi}_1^-$  and  $\gamma \tilde{\chi}_1^+ \tilde{\chi}_1^-$  production at the LC are listed in Table 3.

Component	Description
SVX	Silicon vertex detector from close to beam pipe to $\sim 11$ cm.
CT	Central tracker starting just past SVX.
PS	Pre-shower just outside the tracker.
EC	Electromagnetic calorimeter.
HC	Hadronic calorimeter.
TOF	Time-of-flight measurement after HC and just before MC.
MC	Muon chamber with first layer after the HC and just beyond the TOF.

Table 2: Summary of detector components referred to in the text.

Assuming that only the  $\tilde{\chi}_1^0$  and  $\tilde{\chi}_1^\pm$  are light, SUSY particle production will be primarily in the final states  $\tilde{\chi}_1^+ \tilde{\chi}_1^-$ ,  $\gamma \tilde{\chi}_1^+ \tilde{\chi}_1^-$ , and (when not phase space limited)  $W^\mp \tilde{\chi}_1^0 \tilde{\chi}_1^\pm$ . (The  $\gamma \tilde{\chi}_1^0 \tilde{\chi}_1^0$  cross section is suppressed due to the small  $Z \tilde{\chi}_1^0 \tilde{\chi}_1^0$  coupling.) The possibilities for SUSY detection depend largely upon which aspects (if any) of a  $\tilde{\chi}_1^\pm$  in the final state are visible [2, 3, 4], which in turn depends almost entirely on  $\Delta m_{\tilde{\chi}}$ . We distinguish several interesting ranges for  $\Delta m_{\tilde{\chi}}$ :

- $\Delta m_{\tilde{\chi}} < m_\pi$ : the  $\tilde{\chi}_1^\pm$  yields a ‘stable particle’ LHIT and/or DIT track and is easily detected:  $\tilde{\chi}_1^+ \tilde{\chi}_1^-$  production will be easily seen.
- $m_\pi < \Delta m_{\tilde{\chi}} < 1$  GeV: the  $\tilde{\chi}_1^\pm \rightarrow \tilde{\chi}_1^0 \pi^\pm$  decay yields a soft  $\pi$  track, possibly in association with a STUB ( $\Delta m_{\tilde{\chi}} < 180$  MeV) or HIP ( $\Delta m_{\tilde{\chi}} < 1$  GeV) signature. Direct  $\tilde{\chi}_1^+ \tilde{\chi}_1^-$  production then yields a  $\cancel{E} + \pi\pi$  final state, where the  $\cancel{E}$  is associated with the  $\tilde{\chi}_1^0$ 's. Since the  $\pi$ 's are very soft, backgrounds to this final state from  $\gamma\gamma$ -induced interactions are very large, and it is unlikely that the  $\pi^+\pi^-$  SUSY signal can be isolated. One must tag  $\tilde{\chi}_1^+ \tilde{\chi}_1^-$  production using  $e^+e^- \rightarrow \gamma \tilde{\chi}_1^+ \tilde{\chi}_1^-$ , leading to a  $\gamma + \cancel{E} + \pi\pi$  final state, or employ the more kinematically limited  $W^\mp \tilde{\chi}_1^0 \tilde{\chi}_1^\pm \rightarrow (\ell^\mp, q' \bar{q}) + \cancel{E} + \pi^\pm$  final states.

Signal	Definition
LHIT	At least one long, heavily-ionizing ( $\geq 2$ MIP's as measured by SVX+CT+PS), large- $p_T$ track that reaches the MC. The energy deposit in the HC in the track direction must be consistent with expected ionization energy deposit for the $\beta$ measured (using TOF and/or SVX+CT+PS), i.e. no hadronic energy deposit.
TOF	At least one large- $p_T$ track seen in the SVX and CT along with a signal in the TOF delayed by 500 ps or more (vs. a particle with $\beta = 1$ ). HC energy deposit (in the direction of the track) is required to be consistent with the ionization expected for the measured $\beta$ , i.e. no large hadronic deposit.
DIT	At least one isolated, large- $p_T$ track in the SVX and CT that fails to reach the MC and deposits energy in the HC no larger than that consistent with ionization energy deposits for the measured (using SVX+CT+PS) $\beta$ . Heavy ionization in the SVX+CT+PS, corresponding to $\beta < 0.8$ or $\beta < 0.6$ (DIT8 or DIT6), may be required. Large $\cancel{E}$ .
KINK	At least one track that terminates in the CT, turning into a soft, but visible, charged-pion daughter-track at a substantial angle to parent. Large $\cancel{E}$ .
STUB	At least one isolated, large- $p_T$ (as measured using SVX) track that registers in all SVX layers, but does not pass all the way through the CT. Energy deposits in the EC and HC in the direction of the track should be minimal. Large $\cancel{E}$ .
SNT	One or more STUB tracks and large $\cancel{E}$ with no additional trigger. Heavy ionization of the STUB in the SVX corresponding to $\beta < 0.8$ (SNT8) is required.
S $\gamma$	One or more STUB tracks and large $\cancel{E}$ with a $p_T^\gamma > 10$ GeV trigger. Heavy ionization of the STUB in the SVX corresponding to $\beta < 0.8$ (S $\gamma$ 8) is required.
HIP	At least one high-impact-parameter ( $b \geq 5\sigma_b$ ) soft pion track in the SVX, with $p_T^\gamma > 10$ GeV triggering and large $\cancel{E}$ , perhaps in association with a visible KINK in the SVX.
$\gamma + \cancel{E}$	Isolated, large- $E_T$ photon and large $\cancel{E}$ . Relevant if the soft $\pi$ 's cannot be detected.
mSUGRA-like	jets or leptons + $\cancel{E}$

Table 3: Summary of signals for  $\tilde{\chi}_1^+ \tilde{\chi}_1^-$  and  $\gamma \tilde{\chi}_1^+ \tilde{\chi}_1^-$  production. MIP refers to a minimally-ionizing-particle such as a highly relativistic muon. For detector component notation, see Table 2.

- $1 \text{ GeV} < \Delta m_{\tilde{\chi}} < 2 \text{ GeV}$ : the  $\tilde{\chi}_1^\pm$  decays with roughly equal probability to  $\tilde{\chi}_1^0 \pi^\pm$ ,  $\tilde{\chi}_1^0 \pi^\pm \pi^0$  and  $\tilde{\chi}_1^0 \ell^\pm \nu$  ( $\ell = e, \mu$ ). The pion(s) or charged lepton will be rather soft and a  $\gamma$  tag will probably still be necessary to eliminate backgrounds.
- $\Delta m_{\tilde{\chi}} > 2 - 3 \text{ GeV}$ : the  $\tilde{\chi}_1^\pm$  decays either to  $\tilde{\chi}_1^0$ +multi-pion modes at the low end which start to resolve into jets at the higher end or to  $\tilde{\chi}_1^0 \ell^\pm \nu$ . The visible decay products are sufficiently energetic that  $\gamma\gamma$  induced backgrounds can be rejected (using a combination of event topology and  $\cancel{E}$ ) to the extent necessary for mSUGRA-like mode detection of direct  $e^+e^- \rightarrow \tilde{\chi}_1^+ \tilde{\chi}_1^-$  production.

Sensitivity of LEP2 detectors to these various signatures was sufficient to exclude [18, 19]: (a)  $m_{\tilde{\chi}_1^\pm} < \sqrt{s}/2$  in the ‘stable’ and ‘standard’ regions of  $\Delta m_{\tilde{\chi}}$ ; and (b)  $m_{\tilde{\chi}_1^\pm} < 80 \text{ GeV}$  (assuming the  $\tilde{\nu}_e$  is heavy) in the  $m_\pi \leq \Delta m_{\tilde{\chi}} \leq 2 \text{ GeV}$  region. In particular, the backgrounds to the ‘stable’ and  $\gamma$ -tag+ $\cancel{E}$ +soft- $\pi$  signals are very small. In our analysis, we assume that they can continue to be neglected relative to our signal rates at the LC after simple cuts. For the  $\gamma$ -tag+soft- $\pi$  signal, this may, at first sight, seem problematical given that the signal cross section declines with increasing  $s$ , whereas the two-photon ( $\gamma^* \gamma^*$ ) collision backgrounds tend to increase logarithmically with  $s$ . Below, we review the simple cuts that are likely to be very effective in eliminating the two-photon backgrounds.

It is first important to understand the kinematics of the signal. We will trigger on a photon with  $p_T^\gamma > 10 \text{ GeV}$  and  $10^\circ < \theta_\gamma < 170^\circ$ ,  $10^\circ$  being the angle at which electromagnetic coverage by the detector is expected to begin. We will require that  $M_{\chi\chi}^2 = (p_{e^+} + p_{e^-} - p_\gamma)^2$ , the invariant mass-squared of the  $\tilde{\chi}_1^+ \tilde{\chi}_1^-$  pair, be such that  $M_{\chi\chi} > 2m_{\tilde{\chi}_1^\pm}$  when searching for  $\tilde{\chi}_1^\pm$ 's of a certain mass. Of course, the search will start at  $m_{\tilde{\chi}_1^\pm} > 80 \text{ GeV}$ , the LEP2 limit. Most of  $M_{\chi\chi}$  will be invisible, being carried by the  $\tilde{\chi}_1^0 \tilde{\chi}_1^0$  pair. The  $\pi^+$  and  $\pi^-$  in the final state will be very soft, with energies basically set by the size of  $\Delta m_{\tilde{\chi}}$ , and largely central, with some bias for the  $\pi^+$  ( $\pi^-$ ) to move in the direction of the  $e^-$  ( $e^+$ ) beam. Thus, they will tend to be somewhat back-to-back. However, their angle of acoplanarity will be very uniformly distributed. Finally, the  $p_T^\gamma$  of the trigger photon will be clustered at the lowest allowed values and will be primarily balanced by the missing transverse momentum,  $\cancel{p}_T$ , carried by the  $\tilde{\chi}_1^0$ 's.

There are two different types of two-photon background to the  $\gamma + \pi^+ \pi^- + \cancel{E}$  final state of interest. First, there are  $e^+e^- \rightarrow \gamma + e^+e^- + \gamma^* \gamma^* \rightarrow \gamma + e^+e^- + X$ , with  $X = \pi^+ \pi^-$ , reactions in which the final  $e^+$  and  $e^-$  are *both* lost down the beam pipes and, thereby, provide the large missing energy and missing mass associated with the  $\tilde{\chi}_1^0 \tilde{\chi}_1^0$  pair in the signal reaction. If we trigger on (i.e. tag) a photon with substantial  $p_T^\gamma$ , either the  $e^-$  or the  $e^+$  will be given a sufficient transverse kick that it will be detected. To be precise, we define  $\theta_d$  to be the angle above which an electron or positron can be detected. The largest transverse momentum,  $p_T^{\text{max}}$ , that can be carried by the final  $e^+e^-$  pair without one being detected arises when the final  $e^+$  and  $e^-$  are coplanar, have relative  $\phi = 0$  and have polar angles with respect to their respective beams,  $\theta^+$  and  $\theta^-$ , both equal to  $\theta_d$ :  $p_T^{\text{max}} = (E^+ + E^-) \sin \theta_d$ . Using the constraint  $E^+ = \sqrt{s} - E^- - E^\gamma - E^X$ , we have  $p_T^{\text{max}} = (\sqrt{s} - E^X - E^\gamma) \sin \theta_d$ . Meanwhile, the smallest  $p_T$  of the the  $\gamma + X$  system in the final state is  $p_T^{\text{min}} = p_T^\gamma - p_T^X$ , where  $p_T^X$  denotes the magnitude of the  $X$  system transverse momentum.  $p_T^{\text{min}} < p_T^{\text{max}}$  is required to avoid detection of both the final  $e^+$  and  $e^-$ . This

condition can be rewritten in the form

$$p_T^\gamma < \frac{(\sqrt{s} - E^X) \sin \theta_d + p_T^X}{1 + \sin \theta_d}. \quad (1)$$

For the scenario under consideration,  $E^X$  and  $p_T^X$  are of order  $\Delta m_{\tilde{\chi}}$  times a modest boost factor, and do not exceed 1 GeV for the scenarios of interest. Thus, if we impose a  $p_T^\gamma$  cut that exceeds  $\sqrt{s} \frac{\sin \theta_d}{1 + \sin \theta_d}$  then this background process cannot contribute. Current detector plans are consistent with instrumenting the beam hole down to  $\theta_d \sim 1^\circ$ , for which a cut of  $p_T^\gamma > 0.0172\sqrt{s}$  will suffice. For  $\sqrt{s} = 600$  GeV, we would require  $p_T^\gamma > 10.3$  GeV, which motivates our nominal minimal cut of  $p_T^\gamma > 10$  GeV. With this cut, the only way in which an  $e^+e^- \rightarrow \gamma + e^+e^- + X$  process can contribute to the  $\gamma + \pi^+\pi^- + \cancel{E}$  final state of interest is if  $X$  itself contains missing energy of magnitude approaching the magnitude of the minimum  $p_T^\gamma$  being required. One candidate is  $X = \tau^+\tau^- \rightarrow \pi^+\pi^-\nu\bar{\nu}$ , where the  $\tau^+\tau^-$  invariant mass is large enough that the mass and momentum of the  $\nu\bar{\nu}$  system is at least 2 to 3 GeV. However, the  $\pi^+$  and  $\pi^-$  will tend to be much more energetic than expected in the signal reaction (unless  $\Delta m_{\tilde{\chi}} > 500$  MeV) and will tend to be produced more forward and backward (with correlations with the beam directions opposite that expected for the signal) because of the  $t$ -channel  $\tau$  exchange in the Feynman diagram that gives rise to  $\gamma^*\gamma^* \rightarrow \tau^+\tau^-$ . Further, the background from this process can be independently measured using the  $\tau \rightarrow \rho\nu$  decay modes, and then subtracted. Another candidate is  $X = \pi^+\pi^-Z(\rightarrow \nu\bar{\nu})$  for which  $e^+e^- \rightarrow \gamma + e^+e^- + X$  has a small cross section. In events of this type, virtualities are large and the  $\pi$ 's produced will tend to be very energetic and largely forward and backward, whereas the  $\pi$ 's from the signal reaction are quite central and quite soft in the lab frame. Cuts that require soft central pions will thus be very effective in eliminating such backgrounds while retaining almost all the signal events.

A second type of two-photon background arises from overlapping  $e^+e^- \rightarrow \gamma\cancel{E}$  (e.g.  $\gamma Z^*(\rightarrow \nu\bar{\nu})$ , with  $m_{Z^*} > M_{\chi\chi}$ ) and  $e^+e^- \rightarrow e^+e^-\gamma^*\gamma^* \rightarrow e^+e^-\pi^+\pi^-$  collisions in which the final  $e^+e^-$  of the 2nd reaction are allowed to disappear down the beam lines regardless of  $p_T^\gamma$ . At TESLA, with large bunch separation, the two  $e^-$ 's must come from the same  $e^-$  bunch and the two  $e^+$ 's from the same  $e^+$  bunch. Note that a cut requiring large  $\cancel{E}$ , in particular large  $M \sim M_{\chi\chi}$ , can only be satisfied if the  $\cancel{E}$  comes from the same reaction as the  $\gamma$ . The 'hard' process will have a small cross section. Further, the  $\pi$ 's from the overlapping two-photon event tend to be very energetic and the cut requiring central/soft  $\pi$ 's will be very effective (and essentially 100% efficient for the signal events). Further, the  $\pi^+$  and  $\pi^-$  produced in the 2nd collision will tend to balance each other in transverse momentum, whereas this will never be the case for the  $\pi$ 's from the signal events. In addition, for most such events there would be substantial separation in  $z$  (displacement along the beam line) between the two overlapping events. The LC vertex detectors will have exceptional ability to determine the  $z$  vertex location of the event producing the  $\pi$ 's, assuming  $c\tau$  for the  $\tilde{\chi}_1^\pm$  decay is not large. (If it is large, observation of large transverse impact parameters for the  $\pi$ 's would, alone, be sufficient to eliminate any background.) The  $z$  location of the collision producing the  $\gamma$  will hinge on electromagnetic calorimetry and will require a pre-shower plane for good accuracy. We are uncertain of what resolution to expect here, but it could be sufficiently good that a non-zero  $z$  separation would be seen for most overlapping collisions, which could be used to eliminate most of this background.

Another cut that is useful<sup>1</sup> for eliminating two photon backgrounds is to require that the missing energy vector  $\vec{p} = \vec{p}_{e^+} + \vec{p}_{e^-} - \vec{p}_\gamma - \vec{p}_{\pi^+} - \vec{p}_{\pi^-}$  have an angle of  $> 100$  mrad with respect to both beam axes. In fact, our cuts of  $p_T^\gamma > 10$  GeV and  $10^\circ < \theta_\gamma < 170^\circ$  guarantee that this is the case for all signal events; indeed, all but a tiny fraction of the events have an angle between  $\vec{p}$  and both beam axes of  $> 200$  mrad.

In the absence of a reliable Monte Carlo for generating these types of backgrounds, it is impossible to be absolutely certain that a collection of small contributions will not add up to a non-negligible result. The true background level will probably only be known once data taking has begun. If a background is found for our minimal tag requirements of  $p_T^\gamma > 10$  GeV,  $10^\circ \leq \theta_\gamma \leq 170^\circ$  balanced by large missing mass and soft central pions, the  $p_T^\gamma$  cut, can, for  $m_{\tilde{\chi}_1^\pm}$  not too near  $\sqrt{s}/2$ , be increased to the point where the background disappears. For  $L = 1 \text{ ab}^{-1}$  of integrated luminosity, this will typically have little impact on our ability to discover  $\gamma\tilde{\chi}_1^+\tilde{\chi}_1^-$  production and determine  $m_{\tilde{\chi}_1^\pm}$  and  $\Delta m_{\tilde{\chi}}$ . In fact, one very good set of procedures for the latter determinations, discussed in a later section, focuses on events for which the photon energy is near maximal and the invariant mass of the  $\tilde{\chi}_1^+\tilde{\chi}_1^-$  system is very close to  $2m_{\tilde{\chi}_1^\pm}$ . In this kinematic region, backgrounds will surely be negligible unless  $m_{\tilde{\chi}_1^\pm}$  is close to  $\sqrt{s}/2$  (implying that there is no kinematic room for increasing the photon tag requirements). To be more quantitative, we show in Fig. 1 the unpolarized beam and right-handed polarized  $e^-$  beam cross sections as a function of the minimum  $p_T^\gamma$  accepted. Results are shown for the representative cases of  $m_{\tilde{\chi}_1^\pm} = 175, 250, 290$  GeV and  $\mu = 300, 600$  GeV. In the unpolarized case,  $L = 1 \text{ ab}^{-1}$  gives acceptable event rates for discovery (we assume 10 events will be adequate if there is no background) even for very large  $p_T^\gamma$  cuts so long as  $m_{\tilde{\chi}_1^\pm} \lesssim 275$  GeV. As discussed in a later section, these event rates for large  $p_T^\gamma$  are also quite adequate and, indeed, very useful for precise determinations of  $m_{\tilde{\chi}_1^\pm}$  and  $\Delta m_{\tilde{\chi}}$  for such  $\tilde{\chi}_1^\pm$  masses. (The ability to determine  $m_{\tilde{\chi}_1^\pm}$  from the event rate as a function of the  $p_T^\gamma$  cut is immediately apparent from the figure.) At  $m_{\tilde{\chi}_1^\pm} = 290$  GeV, a cut of  $p_T^\gamma > 17$  GeV would still leave a (discoverable rate) of 30 events (for  $L = 1 \text{ ab}^{-1}$ ) if the background is negligible. Determinations of  $m_{\tilde{\chi}_1^\pm}$  and  $\Delta m_{\tilde{\chi}}$  would become less accurate at such a high mass. In the polarized case, event rates are very sensitive to the  $\mu$  parameter. This is good in that it provides important sensitivity to the  $\mu$  (and  $M_2$ ) SUSY parameters, as described in a later section. However, Fig. 1 makes clear that the polarized cross sections are not necessarily large enough to be accurately measured and might not be observable at all. Use of the polarized cross sections will, in many cases, require that the background really is very small starting at  $p_T^\gamma \sim 10 - 20$  GeV. Finally, we note that the results of Fig. 1 assume that the amplitude contribution from the sneutrino exchange diagram is small. If the sneutrino mass is at or below  $\sqrt{s}$ , there will be substantial suppression of the cross section due to the  $\tilde{\nu}_e$  exchange diagram.

We reemphasize the fact, apparent explicitly in Fig. 2 (discussed in the following section), that there is a high probability that one or both of the pions in the  $\gamma\tilde{\chi}_1^\pm\tilde{\chi}_1^-$  final state will have an observable impact parameter whenever  $\Delta m_{\tilde{\chi}}$  is below  $\sim 1$  GeV and  $m_{\tilde{\chi}_1^\pm}$  is in the  $m_{\tilde{\chi}_1^\pm} \lesssim 200$  GeV region, as preferred for the ( $\delta_{GS} = 0$  O-II)/AMSB boundary conditions. In this case, backgrounds will unquestionably be negligible and all the parameter determination studies described later will be possible with the described precisions.

---

<sup>1</sup>We thank H.-U. Martyn for pointing this out.

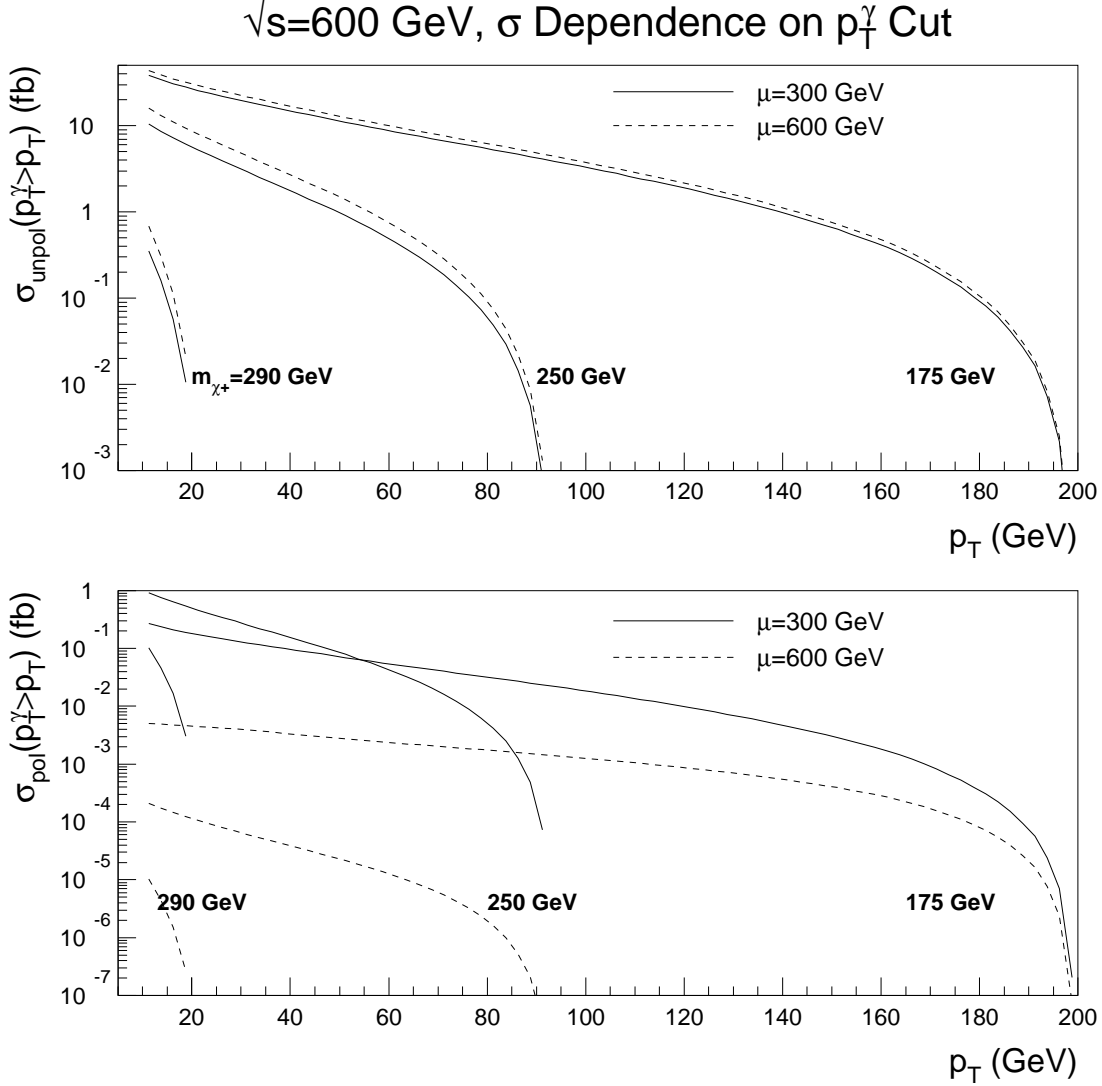


Figure 1: The  $\sqrt{s} = 600$  GeV cross sections for  $\gamma\tilde{\chi}_1^+\tilde{\chi}_1^-$  production as a function of the minimum photon  $p_T^\gamma$ . The results for an unpolarized and a right-handed polarized  $e^-$  beam are shown in the upper and lower plots, respectively, for the cases of  $m_{\tilde{\chi}_1^\pm} = 175, 250, 290$  GeV and  $\mu = 300, 600$  GeV, with  $\tan\beta = 5$ . Cross sections are computed requiring  $10^\circ \leq \theta_\gamma \leq 170^\circ$ . These results assume that the sneutrino exchange diagram can be neglected.

Finally, we return to the possibility of using  $e^+e^- \rightarrow W^\mp\tilde{\chi}_1^\pm\tilde{\chi}_1^0$  in which the  $W$  can decay either leptonically or hadronically and  $\tilde{\chi}_1^\pm \rightarrow \pi^\pm\tilde{\chi}_1^0$ . For moderate  $m_{\tilde{\chi}_1^\pm}$ , the cross section for the production process is quite substantial. For example, for  $m_{\tilde{\chi}_1^\pm} = 175$  GeV,  $\tan\beta = 5$ ,  $\mu = 600$  GeV and  $\sqrt{s} = 600$  GeV (450 GeV), the unpolarized beam cross section is 12 fb (0.46 fb) and the pure  $e_R^-$  cross section is 0.28 fb



(0.007 fb), after summing over both  $W^-\tilde{\chi}_1^+\tilde{\chi}_1^0$  and  $W^+\tilde{\chi}_1^-\tilde{\chi}_1^0$  production. The  $\sqrt{s} = 600$  GeV cross sections (for instance) are to be compared to the  $p_T^\gamma > 10$  GeV cross sections of Fig. 1: 38.5 fb for unpolarized beams and 0.27 fb for pure  $e_R^-$ . The  $W^\mp\tilde{\chi}_1^\pm\tilde{\chi}_1^0$  cross section is thus substantial so long as  $2m_{\tilde{\chi}_1^\pm} + m_W$  is not too near  $\sqrt{s}$ . This production mode could certainly be considered as an alternative for discovery and parameter studies if the  $\gamma\tilde{\chi}_1^+\tilde{\chi}_1^-$  mode should (contrary to our expectation) have significant background. We have not studied possible backgrounds to the  $W^\mp\tilde{\chi}_1^\pm\tilde{\chi}_1^0$  channels, although we expect backgrounds to be small. We will only remark on its possible utility in a few places.

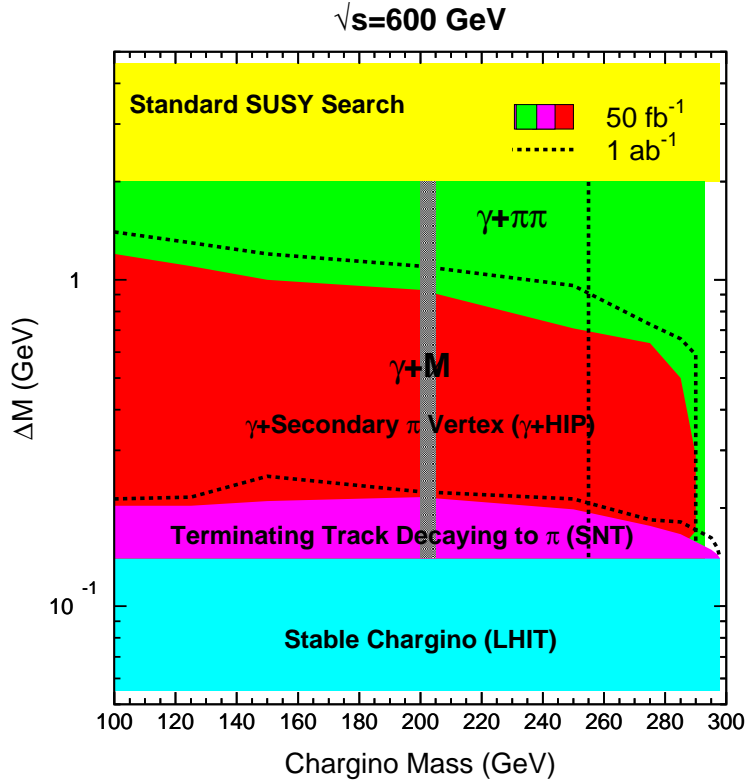


Figure 2: Regions in  $\Delta m_{\tilde{\chi}}, m_{\tilde{\chi}_1^\pm}$  parameter space for which different discovery modes are viable. The SNT,  $\gamma$ +HIP and  $\gamma + \pi\pi$  modes are presumed to be background free; we assume that 10 events will be adequate for discovery. For the SNT,  $\gamma$ +HIP and  $\gamma + \cancel{M}$  signals, discovery reach is given for  $L = 50 \text{ fb}^{-1}$  and also for  $L = 1 \text{ ab}^{-1}$ . Also shown by the vertical band and vertical line (the band for  $L = 50 \text{ fb}^{-1}$  and the line for  $L = 1 \text{ ab}^{-1}$ ) is the reach of the  $\gamma + \cancel{M}$  detection mode, which is relevant only if the soft  $\pi$ 's are not detectable, as might be the case for some range of  $\Delta m_{\tilde{\chi}} \gtrsim 200$  MeV. (Limits in this mode assume  $S/\sqrt{B} > 5$  and  $S/B > 0.02$  is required; see text.) Note the large increase in discovery reach for the  $\gamma + \cancel{M}$  mode with increased  $L$ .

**3. Discovery Reach.** Following the above discussion, we can estimate the regions in  $(\Delta m_{\tilde{\chi}}, m_{\tilde{\chi}_1^\pm})$  parameter space for which the various SUSY discovery modes will be viable at a  $\sqrt{s} = 600$  GeV LC. They

are shown in Fig. 2. For  $\Delta m_{\tilde{\chi}} \gtrsim 2$  GeV, we assume (following the LEP experience) that observation of  $\tilde{\chi}_1^+ \tilde{\chi}_1^-$  production will be possible up to very nearly  $m_{\tilde{\chi}_1^\pm} \sim \sqrt{s}/2$ . For  $\Delta m_{\tilde{\chi}} < m_\pi$ , the  $\tilde{\chi}_1^\pm$  will be sufficiently stable in the detector that an LHIT signal for  $\tilde{\chi}_1^+ \tilde{\chi}_1^-$  production will be easily detected up to threshold. For  $\Delta m_{\tilde{\chi}}$  between  $m_\pi$  and roughly 200 MeV, the SNT signal will be viable. In fact, since triggering will not be necessary at the NLC, even (STUB) charged tracks as short as 4 or 5 cm can be directly imaged,<sup>2</sup> implying that our  $\beta < 0.8$  heavy ionization requirement for the SNT signal could be relaxed. For  $200 \text{ MeV} < \Delta m_{\tilde{\chi}} < 2$  GeV, it is very probable that one will need to employ the  $\gamma$  tag signatures, i.e.  $\gamma + \text{HIP}(s)$  and  $\gamma + \pi(s)$  (always with large  $\cancel{E}$ ). We believe that the  $\gamma + \text{HIP}$  and SNT signatures will be background-free. (They disappear at the largest values of  $m_{\tilde{\chi}_1^\pm}$  due to inadequate boost for the produced  $\tilde{\chi}_1^\pm$ , which leads to too small an impact parameter for the HIP or too short a path length for the STUB track.) Development of Monte Carlo programs that can accurately compute the backgrounds to the above signals should be a high priority, especially for the  $\gamma + \cancel{E} + \pi(s)$  ( $\gamma + \pi(s)$  for short) signal. However, the measured background after cuts at LEP2 for the  $\gamma + \pi(s)$  signal was negligible or very small even without requiring a high impact parameter for at least one of the  $\pi$ 's. This, coupled with the arguments given in the previous section allow for some optimism that the background for the  $\gamma + \pi(s)$  signal will continue to be small at high  $\sqrt{s}$ , even for the relatively mild  $p_T^\gamma > 10$  GeV cut. The exact boundaries for the LHIT, SNT,  $\gamma + \text{HIP}(s)$  and  $\gamma + \pi(s)$  signatures shown assume that 10 events are adequate to detect the above signals (assuming no background). The rapid  $s$ -wave threshold turn-on of  $\gamma \tilde{\chi}_1^+ \tilde{\chi}_1^-$  production allows one to probe almost to the  $m_{\tilde{\chi}_1^\pm} \sim \sqrt{s}/2 - p_T^\gamma$  kinematic limit so long as the detector can resolve the soft  $\pi$ 's from the  $\tilde{\chi}_1^\pm$  decays. As shown in Fig. 2, even assuming zero background,  $L = 1 \text{ ab}^{-1}$  does not greatly increase the discovery reach of the STUB and HIP channels as compared to  $L = 50 \text{ fb}^{-1}$ . The increase in reach for  $L = 1 \text{ ab}^{-1}$  for the (stable) LHIT signal is very small and is not shown. Since it is possible that backgrounds that are negligible at  $L = 50 \text{ fb}^{-1}$  result in a non-negligible number of events at  $L = 1 \text{ ab}^{-1}$ , one should not absolutely rely on the indicated increase in coverage for the SNT and  $\gamma + \text{HIP}$  signals for the latter  $L$ .

Given that the boundary conditions in models with loop-dominated gaugino masses are such that  $\Delta m_{\tilde{\chi}} \in [200 \text{ MeV}, 2 \text{ GeV}]$  is almost a certainty, the reach of the  $\gamma$ -tag+ $\cancel{E}$ +soft- $\pi$ 's (with or without HIP(s)) signal is of great importance. If the soft pions cannot be detected/tracked before they curl up (e.g. because the magnetic field is too strong), then sensitivity to  $\gamma \tilde{\chi}_1^+ \tilde{\chi}_1^-$  production will be much more limited. (This is illustrated by the somewhat higher  $m_{\tilde{\chi}_1^\pm}$  limits of L3 vs. DELPHI for  $\Delta m_{\tilde{\chi}} \in [200 \text{ MeV}, 2 \text{ GeV}]$  due to the fact that L3's magnetic field is weaker than DELPHI's.) If the  $\pi^\pm$  tracks are not detected, one important signal is  $e^+e^- \rightarrow \gamma \tilde{\chi}_1^+ \tilde{\chi}_1^- \rightarrow \gamma + \text{invisible}$ , for which the  $e^+e^- \rightarrow \gamma \nu \bar{\nu}$  background is substantial. For any given presumed value of  $m_{\tilde{\chi}_1^\pm}$ , we place a cut on the invisible mass,  $M$ , recoiling opposite the trigger photon of at least  $M > 2m_{\tilde{\chi}_1^\pm}$ , that removes much of the  $\nu \bar{\nu}$  background, in particular that from on-shell  $\gamma + Z$  production. The more limited discovery reach is illustrated by the  $\gamma + M$  boundaries (one for  $L = 50 \text{ fb}^{-1}$  and one for  $L = 1 \text{ ab}^{-1}$ ) drawn at fixed  $m_{\tilde{\chi}_1^\pm}$  for  $\Delta m_{\tilde{\chi}} \in [200 \text{ MeV}, 2 \text{ GeV}]$  in Fig. 2. For

---

<sup>2</sup>We thank M. Peskin for bringing this to our attention.

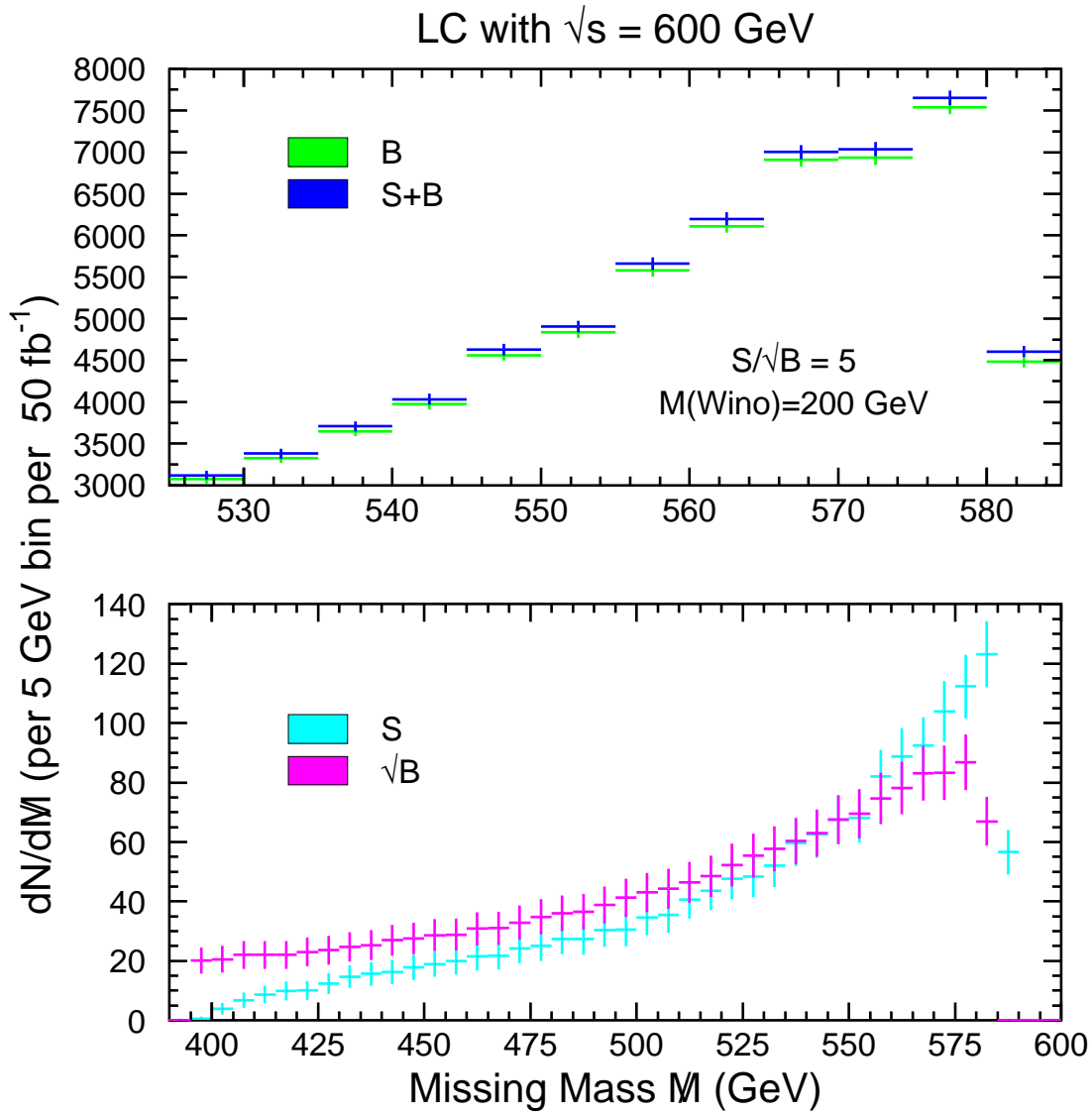


Figure 3:  $dN/dM$  for signal and background in the  $\gamma + M$  final state using 5 GeV bins and assuming  $L = 50 \text{ fb}^{-1}$ . Also shown are  $S$  and  $\sqrt{B}$ .

lower  $m_{\tilde{\chi}_1^\pm}$  values, cuts can be placed on  $M$  so as to obtain  $S/B \geq 0.02$  and  $S/\sqrt{B} \geq 5$  for  $L = 50 \text{ fb}^{-1}$ . The difficulty of observing the signal for large  $m_{\tilde{\chi}_1^\pm}$  can be seen from the  $m_{\tilde{\chi}_1^\pm} = 200$  GeV,  $L = 50 \text{ fb}^{-1}$  results shown in Fig. 3. The upper part of the figure gives  $S$  and  $S+B$  in 5 GeV bins in the  $M > 525$  GeV region. The lower part of the figure shows  $S$  and  $\sqrt{B}$  for 5 GeV bins. We see that  $S/\sqrt{B}$  per bin is only of order 1 for  $M > 525$  GeV. Although at the peak in  $S$ , located at  $M \sim 580$  GeV, the 5 GeV bin has  $S/B = 0.028$ , for  $L = 50 \text{ fb}^{-1}$  this one bin only yields  $S/\sqrt{B} = 1.87$ . Thus, for this  $L$  it is necessary to include all the bins with  $M \geq 525$  GeV in order to get a net  $S/\sqrt{B} > 5$  signal; in this case the net  $S/B$  is

$\sim 0.02$ . However, with higher  $L$  one can do much better by focusing on the highest  $M$  bins for which  $S/B$  is largest. In Table 4 we give the  $\gamma + M$  cross section  $\sigma$  as a function of  $m_{\tilde{\chi}_1^\pm}$  for  $580 \text{ GeV} \leq M \leq 590 \text{ GeV}$ ,

$m_{\tilde{\chi}_1^\pm}$ (GeV)	175	200	250	260	275	285	290
$\sigma$ (fb)	3.9	3.6	2.3	1.8	1.4	0.90	0.52
$S/B$	0.043	0.040	0.025	0.020	0.016	0.010	0.006
$L$ ( $\text{fb}^{-1}$ ) for $5\sigma$	150	175	435	690	1140	$\sim 3000$	$\sim 8500$

Table 4:  $\gamma + M$  results for  $580 \leq M \leq 590 \text{ GeV}$ .

the ratio  $S/B$ , and the luminosity required for  $S/\sqrt{B} = 5$ . From this table, we see that if  $S/B \gtrsim 0.02$  is required for a viable signal, then  $m_{\tilde{\chi}_1^\pm}$  up to  $\sim 260 \text{ GeV}$  can be probed for  $L \geq 700 \text{ fb}^{-1}$ . If systematics can be controlled to the  $S/B \sim 0.01$  level, then the  $\gamma + M$  signal could be observed up to  $m_{\tilde{\chi}_1^\pm} \sim 285 \text{ GeV}$  for very high  $L \sim 3000 \text{ fb}^{-1}$ .

**4. Determining  $m_{\tilde{\chi}_1^\pm}$  and  $\Delta m_{\tilde{\chi}}$ .** If the chargino or its decay products are directly visible, for expected  $e^+e^-$  collider luminosities it will be possible to detect  $\tilde{\chi}_1^+\tilde{\chi}_1^-$  or  $\gamma\tilde{\chi}_1^+\tilde{\chi}_1^-$  production for  $m_{\tilde{\chi}_1^\pm}$  up to values very close to the  $\sqrt{s}/2$  threshold. The soft  $\pi$ (s) from the  $\tilde{\chi}_1^\pm$  decay or the non-prompt  $\tilde{\chi}_1^\pm$  decay LHIT, SNT and/or  $\gamma$ +HIP signals will indicate clearly that  $\Delta m_{\tilde{\chi}}$  is small. The next important task will be to measure  $m_{\tilde{\chi}_1^\pm}$  and  $\Delta m_{\tilde{\chi}}$  as precisely as possible. We focus entirely on scenarios with  $m_\pi < \Delta m_{\tilde{\chi}} \lesssim 0.8 \text{ GeV}$  for which we must employ the  $\gamma\tilde{\chi}_1^+\tilde{\chi}_1^-$  channel and for which the  $\tilde{\chi}_1^\pm \rightarrow \pi^\pm\tilde{\chi}_1^0$  branching ratio is close to 1. For larger  $\Delta m_{\tilde{\chi}}$ , one would have to take into account the  $\tilde{\chi}_1^\pm \rightarrow \pi^\pm\pi^0\tilde{\chi}_1^0$  and  $\tilde{\chi}_1^\pm \rightarrow \ell^\pm\nu\tilde{\chi}_1^0$  decays. Our techniques could still be applied, but the effective event rates for the  $\pi^\pm\tilde{\chi}_1^0$  channels would be reduced and some accuracy lost unless the other modes could be included in the analysis following analogous procedures (which are relatively straightforward extensions of those presented).

The most direct technique for determining  $m_{\tilde{\chi}_1^\pm}$  and  $\Delta m_{\tilde{\chi}}$  independently of theoretical assumptions is via the  $\pi^\pm$  kinematic distributions. We shall later discuss the determination of  $\Delta m_{\tilde{\chi}}$  via observing a distribution of  $\pi^\pm$  impact parameters. By way of preview, we note that the impact parameter distribution is determined primarily by  $c\tau$  and  $\Delta m_{\tilde{\chi}}$ , with weak dependence on  $m_{\tilde{\chi}_1^\pm}$ . Once  $m_{\tilde{\chi}_1^\pm}$  is determined via the kinematic procedures we shall describe below, in favorable cases (large  $c\tau$ ) the impact parameter distribution will allow a simultaneous determination of  $c\tau$  and  $\Delta m_{\tilde{\chi}}$  with errors on  $\Delta m_{\tilde{\chi}}$  that are competitive with the errors we shall find using kinematic distributions. Of course, the kinematic distribution procedures we now describe are essential when the  $\tilde{\chi}_1^\pm$  decay is simply too prompt to directly observe its path length. However, even if the distribution of path lengths is not very apparent (because most events are clustered at low impact parameter, e.g. as typical for  $\Delta m_{\tilde{\chi}} \sim 800 \text{ MeV}$  for which  $c\tau \sim 190 \mu\text{m}$ ) or useful, most events *will* have an observable non-zero impact parameter for at least one  $\pi$  and, consequently, backgrounds to the  $\gamma + \pi^+\pi^- + \cancel{E}$  signal will certainly be negligible after our simple cuts on  $p_T^\gamma$ ,  $\theta_\gamma$  and  $M_{\chi\chi}$  described earlier.

The observables in the  $\gamma\tilde{\chi}_1^+\tilde{\chi}_1^- \rightarrow \gamma\pi^+\pi^-\tilde{\chi}_1^0\tilde{\chi}_1^0$  final state of interest are the invariant mass of the chargino pair,  $M_{\chi\chi} \equiv \sqrt{(p_{e^+} + p_{e^-} - p_\gamma)^2}$ , and the energies,  $E_\pi^*$ , of the  $\pi$ 's in the  $M_{\chi\chi}$  rest frame. For

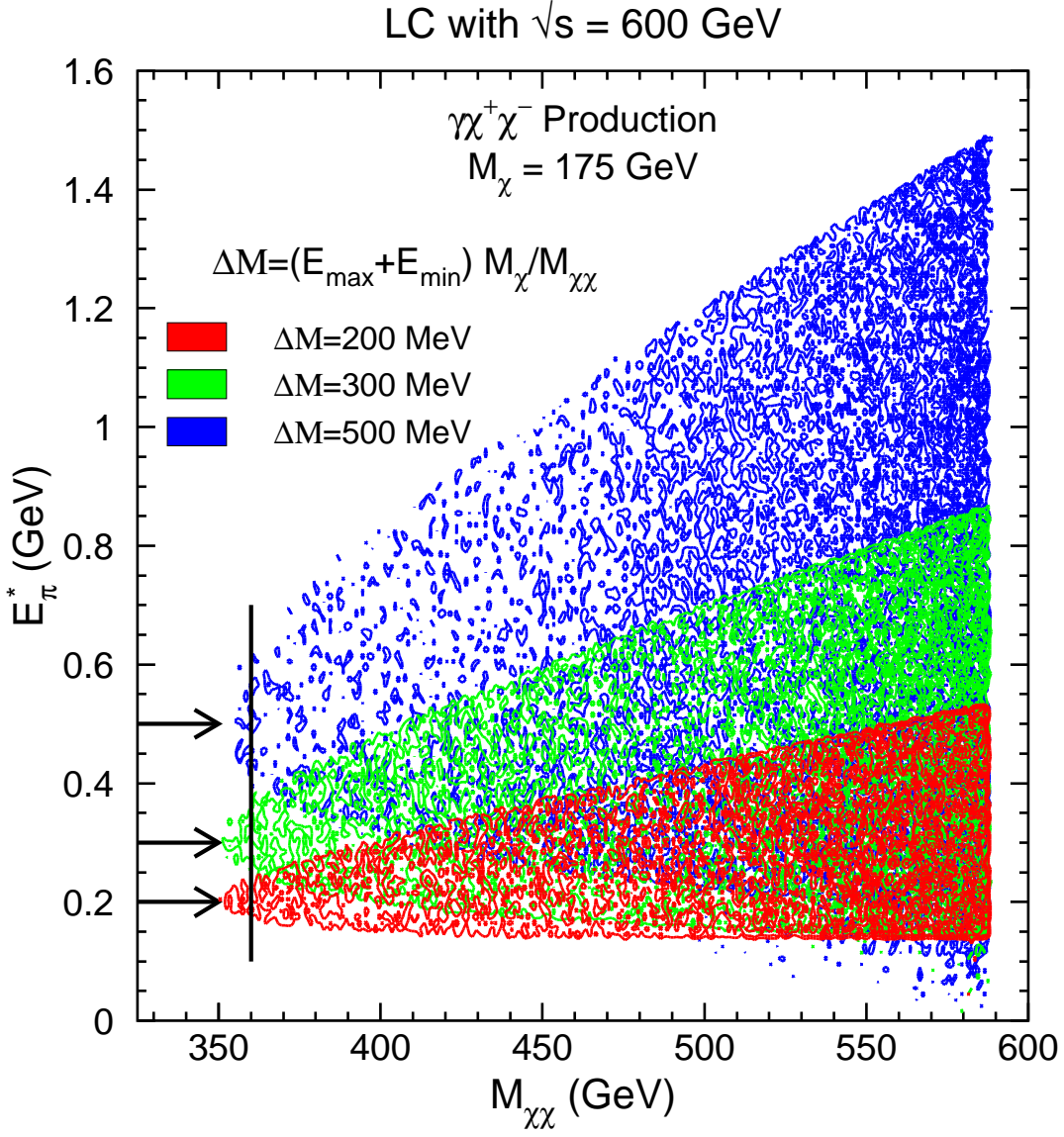


Figure 4: We plot event number contours in  $[M_{\chi\chi}, E_{\pi}^*]$  parameter space for several different values of  $\Delta m_{\tilde{\chi}}$  taking  $m_{\tilde{\chi}_1^\pm} = 150$  GeV. Note the event concentration at high  $M_{\chi\chi}$ . The arrows indicate the values of  $\Delta m_{\tilde{\chi}}$ , which are approximately equal to  $E_{\pi}^*$  at the  $M_{\chi\chi} = 2m_{\tilde{\chi}_1^\pm}$  endpoint. The vertical line at 360 GeV denotes the  $M_{\chi\chi}$  value below which the  $E_{\pi}^*$  distribution is approximately Gaussian.

$M_{\chi\chi} > 2m_{\tilde{\chi}_1^\pm}$ , the  $\tilde{\chi}_1^\pm$  are boosted in the  $M_{\chi\chi}$  rest frame and  $E_{\pi}^*$  depends upon the orientation of  $\vec{p}_{\pi}$  in the  $\tilde{\chi}_1^\pm$  rest frame with respect to the boost direction. The maximum and minimum  $E_{\pi}^*$  values are given by

$$E_{\pi}^*{}^{\max} = \gamma_{\tilde{\chi}_1^\pm}(E_0 + \beta_{\tilde{\chi}_1^\pm} p_0), \quad E_{\pi}^*{}^{\min} = \gamma_{\tilde{\chi}_1^\pm}(E_0 - \beta_{\tilde{\chi}_1^\pm} p_0), \quad (2)$$

with

$$\beta_{\tilde{\chi}_1^\pm} = \sqrt{1 - \frac{4m_{\tilde{\chi}_1^\pm}^2}{M_{\chi\chi}^2}}, \quad \gamma_{\tilde{\chi}_1^\pm} = \frac{1}{\sqrt{1 - \beta_{\tilde{\chi}_1^\pm}^2}}, \quad E_0 = \frac{m_{\tilde{\chi}_1^\pm}^2 + m_\pi^2 - m_{\tilde{\chi}_1^0}^2}{2m_{\tilde{\chi}_1^\pm}} \simeq \Delta m_{\tilde{\chi}}, \quad p_0 = \sqrt{E_0^2 - m_\pi^2} \quad (3)$$

characterizing the charginos in the  $M_{\chi\chi}$  rest frame and the  $\pi^\pm$  in the  $\tilde{\chi}_1^\pm$  rest frames. These equations can be inverted to give

$$\gamma_{\tilde{\chi}_1^\pm}^2 = \frac{\overline{E}^2 + m_\pi^2 - \widehat{E}^2 \pm \sqrt{(\overline{E}^2 + m_\pi^2 - \widehat{E}^2)^2 - 4\overline{E}^2 m_\pi^2}}{2m_\pi^2}, \quad (4)$$

$$m_{\tilde{\chi}_1^\pm} = \frac{M_{\chi\chi}}{2\gamma_{\tilde{\chi}_1^\pm}}, \quad \Delta m_{\tilde{\chi}} = m_{\tilde{\chi}_1^\pm} - \sqrt{m_{\tilde{\chi}_1^\pm}^2 - \frac{2m_{\tilde{\chi}_1^\pm}\overline{E}}{\gamma_{\tilde{\chi}_1^\pm}} + m_\pi^2} \simeq \frac{\overline{E}}{m_{\tilde{\chi}_1^\pm}}, \quad (5)$$

where  $2\overline{E} = E_\pi^{\star \max} + E_\pi^{\star \min}$  and  $2\widehat{E} = E_\pi^{\star \max} - E_\pi^{\star \min}$ . (The  $\simeq$  expressions in Eqs. (3) and (5) apply if we neglect terms of order  $m_\pi^2/m_{\tilde{\chi}_1^\pm}^2$  and  $\Delta m_{\tilde{\chi}}^2/m_{\tilde{\chi}_1^\pm}^2$ .) For any given  $M_{\chi\chi}$ , there is a two-fold ambiguity in  $\gamma_{\tilde{\chi}_1^\pm}^2$ . The  $-$  ( $+$ ) sign applies for lower (higher)  $M_{\chi\chi}$  values. Only one set of choices as a function of  $M_{\chi\chi}$  will lead to  $M_{\chi\chi}$ -independent values for  $m_{\tilde{\chi}_1^\pm}$  and  $\Delta m_{\tilde{\chi}}$ . Even at a fixed  $M_{\chi\chi}$ , fitting the actual distribution in  $E_\pi^*$  can provide a unique determination of  $m_{\tilde{\chi}_1^\pm}$  and  $\Delta m_{\tilde{\chi}}$ , given enough statistics.

Since the  $\pi$ 's are soft, the resolution for measuring  $p_\pi$  in the lab frame will be dominated by the ‘constant’ term, which has a typical value of  $\sim 0.5\%$ . Further,  $\delta M_{\chi\chi}/M_{\chi\chi} \sim \delta E_\gamma \sqrt{s}/M_{\chi\chi}^2 \sim 0.1\sqrt{E_\gamma}\sqrt{s}/M_{\chi\chi}^2$  (all in GeV) will also be very small. We have generated events including the measurement smearing in  $E_\gamma$ . For each event with a given  $M_{\chi\chi}$ , we boost to the  $M_{\chi\chi}$  (i.e. chargino-pair) rest frame and compute the energies,  $E_\pi^*$ , of the observed  $\pi$ 's. In Fig. 4, we show the region of the  $[E_\pi^*, M_{\chi\chi}]$  plane occupied by the events for several different choices of  $\Delta m_{\tilde{\chi}}$ , taking  $m_{\tilde{\chi}_1^\pm} = 175$  GeV. For  $L = 50 \text{ fb}^{-1}$  and  $\sqrt{s} = 600$  GeV, the occupied region will contain  $\sim 5000$  entries (2 entries per event). A large fraction of the entries reside near the large- $M_{\chi\chi}$  boundary.

The location of the threshold in  $M_{\chi\chi}$  provides a particularly useful way to measure  $2m_{\tilde{\chi}_1^\pm}$ . The statistical error for such a determination depends upon the number of events near the threshold. We assume that the  $\gamma + \pi\pi$  signal is background-free and compute the approximate  $1\sigma$  error  $\delta m_{\tilde{\chi}_1^\pm}$  from the criterion:

$$\frac{\widehat{S}(m_{\tilde{\chi}_1^\pm} - \delta m_{\tilde{\chi}_1^\pm}) - \widehat{S}(m_{\tilde{\chi}_1^\pm})}{\sqrt{\widehat{S}(m_{\tilde{\chi}_1^\pm} - \delta m_{\tilde{\chi}_1^\pm})}} = 1, \quad (6)$$

where  $\widehat{S}$  is the number of events in the near-threshold region  $2m_{\tilde{\chi}_1^\pm} \leq M_{\chi\chi} \leq 2m_{\tilde{\chi}_1^\pm} + 10$  GeV. For  $m_{\tilde{\chi}_1^\pm} \in [150, 225]$  GeV ( $\in [250, 275]$  GeV) we find  $\delta m_{\tilde{\chi}_1^\pm} \sim 1$  GeV ( $\sim 0.5$  GeV) for  $L = 50 \text{ fb}^{-1}$  and  $\delta m_{\tilde{\chi}_1^\pm} \sim 0.2$  GeV ( $\sim 0.1$  GeV) for  $L = 1 \text{ ab}^{-1}$ . The accuracy improves at higher masses because of the increasing sharpness of  $d\sigma/dM_{\chi\chi}$  as a function of  $M_{\chi\chi}$ .

The most direct way to determine  $\Delta m_{\tilde{\chi}}$  is to concentrate on the  $M_{\chi\chi} \sim 2m_{\tilde{\chi}_1^\pm}$  region for which  $E_\pi^* \simeq E_0 \simeq \Delta m_{\tilde{\chi}}$ . Because of resolution smearing, there are actually events with  $M_{\chi\chi} < 2m_{\tilde{\chi}_1^\pm}$  and a finite spread to  $E_\pi^*$  in this region. We have examined the  $E_\pi^*$  distribution for two cuts: (I)  $M_{\chi\chi} < 2m_{\tilde{\chi}_1^\pm}$

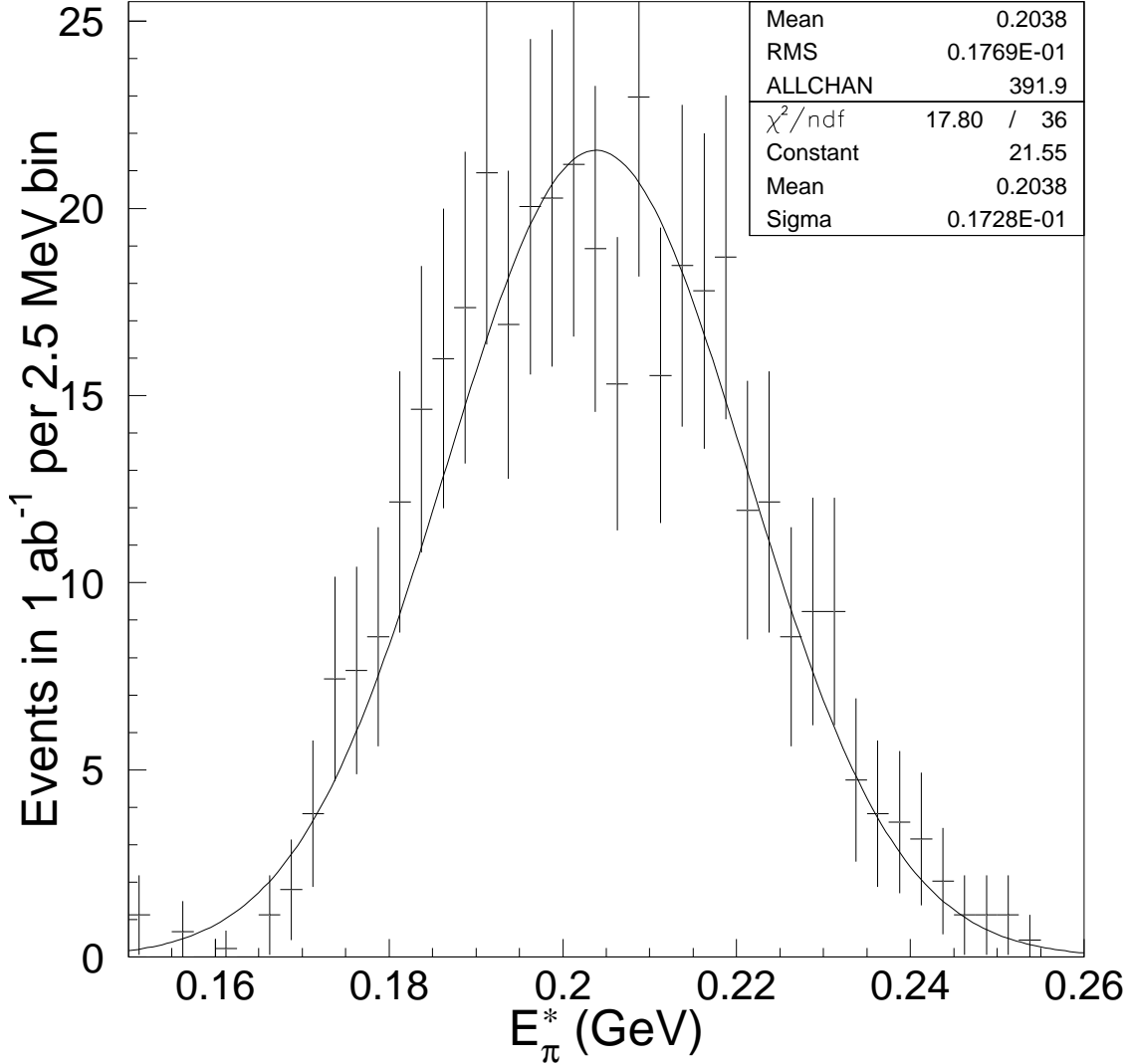


Figure 5: We plot the distribution of  $E_\pi^*$  for the case of  $m_{\tilde{\chi}_1^\pm} = 175$  GeV,  $\Delta m_{\tilde{\chi}} = 200$  MeV and  $M_{\chi\chi} \leq 360$  GeV. Also shown is the Gaussian fit and its r.m.s. used to determine the error for this case in Table 5. We took  $L = 1 \text{ ab}^{-1}$ , yielding 392 events in the plot.

and (II)  $M_{\chi\chi} < 2m_{\tilde{\chi}_1^\pm} + 10$  GeV. For cuts (I), there are fewer events but, for  $\Delta m_{\tilde{\chi}} \lesssim 400$  MeV, the  $E_\pi^*$  distribution is more closely centered on  $\Delta m_{\tilde{\chi}}$ . A typical case is illustrated in Fig. 5, based on cuts (II). The error on  $\overline{E}_\pi^*$ , the average  $\pi$  energy, is given by  $\delta\overline{E}_\pi^*/\sqrt{N}$ , where  $N$  is the number of events and  $\delta\overline{E}_\pi^*$  is estimated as the width of a Gaussian fit to the  $E_\pi^*$  spectrum. Table 5 gives  $\overline{E}_\pi^*$  and  $\delta\overline{E}_\pi^*$  for both  $M_{\chi\chi}$  cuts (I) and (II) for a number of  $m_{\tilde{\chi}_1^\pm}$  and  $\Delta m_{\tilde{\chi}}$  choices assuming  $L = 1 \text{ ab}^{-1}$ .  $L = 50 \text{ fb}^{-1}$  is not adequate to give particularly small errors, but would allow a first determination of  $\Delta m_{\tilde{\chi}}$  to within 10 to 20 MeV or so.

[ $m_{\tilde{\chi}_1^\pm}$ (GeV), $\Delta m_{\tilde{\chi}}$ (MeV)]	$M_{\chi\chi}$ cut I		$M_{\chi\chi}$ cut II	
	$\overline{E}_\pi^*$ (MeV)	$\delta\overline{E}_\pi^*$ (MeV)	$\overline{E}_\pi^*$ (MeV)	$\delta\overline{E}_\pi^*$ (MeV)
[175, 200]	201.6	1.9	203.8	0.9
[175, 300]	303.4	3.4	306.7	1.8
[175, 500]	493.2	9.0	499.0	3.6
[225, 200]	200.6	1.3	203.2	0.7
[225, 300]	300.4	2.6	303.6	1.2
[225, 500]	493.9	6.8	498.3	2.7
[250, 200]	200.4	1.0	202.8	0.5
[250, 300]	299.9	2.1	303.5	1.0
[250, 500]	494.0	5.0	498.2	2.1

Table 5: Summary of  $\overline{E}_\pi^*$  values and errors,  $\delta\overline{E}_\pi^*$ , as a function of  $m_{\tilde{\chi}_1^\pm}$ ,  $\Delta m_{\tilde{\chi}}$  and  $M_{\chi\chi}$  cut, for  $m_{\tilde{\chi}_1^\pm} = 175$ , 225 and 250 GeV and  $\Delta m_{\tilde{\chi}} = 200, 300$ , and 500 MeV, taking  $L = 1 \text{ ab}^{-1}$ .

There is considerable variation of  $\delta\overline{E}_\pi^*$  with the case and the cut. In addition,  $\overline{E}_\pi^*$  is usually not precisely equal to  $\Delta m_{\tilde{\chi}}$ , with shifts ranging up to 7 MeV, depending on the exact case and cuts employed. However, the expected shape for the  $E_\pi^*$  distribution for any given choices of  $m_{\tilde{\chi}_1^\pm}$ ,  $\Delta m_{\tilde{\chi}}$  and  $M_{\chi\chi}$  cut is precisely known (to the extent that the resolutions for  $E_\pi$  and  $E_\gamma$  are known) and the expected shift  $\overline{E}_\pi^* - \Delta m_{\tilde{\chi}}$  can be computed. Our estimate is that one could in the end achieve an uncertainty for  $\Delta m_{\tilde{\chi}}$  of order 2–5 MeV or better in most cases. Once actual data were available, one would take the experimental distribution resulting from the underlying  $m_{\tilde{\chi}_1^\pm}$  and  $\Delta m_{\tilde{\chi}}$  and compare it to a selection of theoretical predictions for the measured  $m_{\tilde{\chi}_1^\pm}$  (using the technique described earlier) and a range of  $\Delta m_{\tilde{\chi}}$  choices and minimize the  $\chi^2$ .

To repeat a point from the introduction, we note that the above  $M_{\chi\chi} \sim 2m_{\tilde{\chi}_1^\pm}$  techniques for determining  $m_{\tilde{\chi}_1^\pm}$  and  $\Delta m_{\tilde{\chi}}$  (and, of course, detecting the charginos in the first place) imply a focus on events with the most energetic photons. Unless  $m_{\tilde{\chi}_1^\pm}$  is quite near  $\sqrt{s}/2$ , the typical photon-tag energy and transverse momentum will be large enough that two-photon (and certainly other) backgrounds to our  $\gamma\pi^+\pi^- \cancel{E}$  final state will surely be negligible even if  $\Delta m_{\tilde{\chi}}$  is large enough that most events do not have an observable HIP for one of the  $\pi$ 's. In contrast, the techniques discussed in the following rely on using the full range of photon tag energies and transverse momenta, and could be compromised if (contrary to our expectation) there is significant background at lower  $E_\gamma, p_T^\gamma$  values when  $\Delta m_{\tilde{\chi}}$  is such that HIP(s) are not observable.

We now compare the above  $M_{\chi\chi} \sim 2m_{\tilde{\chi}_1^\pm}$  results to those obtained by employing the full distribution in  $[M_{\chi\chi}, E_\pi^*]$ , including not only the location of the end-points in the  $E_\pi^*$  spectra as a function of  $M_{\chi\chi}$ , but also the full shape of the distribution. In particular, one could hope to make use of the large number of events at large  $M_{\chi\chi}$ . We now describe two procedures for estimating the resulting errors on  $m_{\tilde{\chi}_1^\pm}$  and



$\Delta m_{\tilde{\chi}}$ . In the first, we consider only the one-dimensional distribution in  $E_{\pi}^*$  as a function of  $m_{\tilde{\chi}_1^{\pm}}$  and  $\Delta m_{\tilde{\chi}}$ . We performed our study for  $m_{\tilde{\chi}_1^{\pm}}$  values centered on 175 GeV and  $\Delta m_{\tilde{\chi}}$  values centered on 200 MeV and employed bins of size 10 MeV (i.e. chosen to be somewhat larger than the resolution for  $E_{\pi}^*$ ). For two choices ( $A$  and  $B$ ) of  $[m_{\tilde{\chi}_1^{\pm}}, \Delta m_{\tilde{\chi}}]$ , we found the maximum difference  $D_{\max}$ , based on the 1-D Kolmogorov-Smirnov (KS) [20] procedure, between the two cumulative distribution functions as a function of  $E_{\pi}^*$  and computed the probability,  $Q_{KS}^{1D} \equiv P(D > D_{\max})$ , that the observed (or more precisely for theoretically computed event rates, the expected) value of  $D_{\max}$  is inconsistent with the two distributions having come from the same parent distribution rather than from two different distributions. The values of  $Q_{KS}^{1D}$  as a function of  $\delta m_{\tilde{\chi}_1^{\pm}} \equiv m_{\tilde{\chi}_1^{\pm}}(A) - m_{\tilde{\chi}_1^{\pm}}(B)$  and  $\delta \Delta m_{\tilde{\chi}} \equiv \Delta m_{\tilde{\chi}}(A) - \Delta m_{\tilde{\chi}}(B)$  are given in Fig. 6 for choices of  $m_{\tilde{\chi}_1^{\pm}}$  and  $\Delta m_{\tilde{\chi}}$  in the ranges  $173 < m_{\tilde{\chi}_1^{\pm}} < 177$  GeV and  $198 < \Delta m_{\tilde{\chi}} < 203$  MeV. Due to the correlation apparent from Eq. (5), which shows that a change in  $\Delta m_{\tilde{\chi}}$  can be compensated by a corresponding change in  $m_{\tilde{\chi}_1^{\pm}}$  without greatly affecting the  $E_{\pi}^*$  distribution, we find that the more direct determination of  $m_{\tilde{\chi}_1^{\pm}}$  from the  $M_{\chi\chi}$  threshold region is crucial, especially for  $L = 50 \text{ fb}^{-1}$ . For  $L = 50 \text{ fb}^{-1}$  ( $L = 1 \text{ ab}^{-1}$ ), a determination of  $m_{\tilde{\chi}_1^{\pm}}$  to within 1 GeV (0.2 GeV) will allow a determination of  $\Delta m_{\tilde{\chi}}$  to within  $\pm 5$  MeV ( $\pm 1$  MeV) at the  $Q_{KS}^{1D} = 0.3$  (roughly  $1\sigma$  exclusion) level.

A generalized KS test can also be applied to the full two-dimensional distribution in the  $[M_{\chi\chi}, E_{\pi}^*]$  plane. (As above, we employ bin sizes of 10 MeV for  $E_{\pi}^*$ . For  $M_{\chi\chi}$ , we employ bins of size 5 GeV, again somewhat larger than expected resolution error.) Results for the resulting  $Q_{KS}^{2D}$  values as a function of  $\delta m_{\tilde{\chi}_1^{\pm}}$  and  $\delta \Delta m_{\tilde{\chi}}$  are given in the bottom two windows of Fig. 6. For  $L = 50 \text{ fb}^{-1}$ , we see that the statistics are somewhat marginal for use of the 2D technique, but a  $\pm 5$  MeV determination of  $\Delta m_{\tilde{\chi}}$  is possible if  $m_{\tilde{\chi}_1^{\pm}}$  is known to within 1 GeV. For  $L = 1 \text{ ab}^{-1}$  the 2D KS test is superior to both the 1D KS test based on binning only in  $E_{\pi}^*$  and the near-threshold technique. Using only the 2D KS test, we find that both  $m_{\tilde{\chi}_1^{\pm}}$  and  $\Delta m_{\tilde{\chi}}$  can be measured with good precision. In particular, the  $Q_{KS}^{2D} > 0.3$  region is confined to  $\delta m_{\tilde{\chi}_1^{\pm}} < 1$  GeV,  $-1 < \delta \Delta m_{\tilde{\chi}} < 2$  MeV. If we combine the 2D KS analysis with the  $M_{\chi\chi}$  threshold determination of  $m_{\tilde{\chi}_1^{\pm}}$ , we do even better. In particular, the  $M_{\chi\chi}$  threshold determination of  $m_{\tilde{\chi}_1^{\pm}}$  to within 0.2 GeV in the  $L = 1 \text{ ab}^{-1}$  case, implies a reduced range of  $-1 < \delta \Delta m_{\tilde{\chi}} < 1$  MeV at the  $Q_{KS}^{2D} = 0.3$  level.

Let us now return to the impact parameter distribution for the  $\pi^{\pm}$  in the final state and the extent to which it can be used to determine  $\Delta m_{\tilde{\chi}}$ ,  $c\tau$  and underlying SUSY parameters. For  $\Delta m_{\tilde{\chi}} \lesssim 800$  MeV, the  $\gamma$ +HIP(s) signature typically has substantial rate. We focus on the distribution of  $\pi^{\pm}$  *transverse* impact parameters,  $b_T$ ,<sup>3</sup> using the central reference case of  $m_{\tilde{\chi}_1^{\pm}} = 175$  GeV,  $\Delta m_{\tilde{\chi}} = 200$  MeV and  $c\tau = 23.81$  mm (the nominal value from Table 1, based on Ref. [2], for the given  $\Delta m_{\tilde{\chi}}$  value). We generate  $e^+e^- \rightarrow \gamma\tilde{\chi}_1^+\tilde{\chi}_1^- \rightarrow \gamma\pi^+\pi^- \cancel{E}$  events at  $\sqrt{s} = 600$  GeV, using the minimal  $p_T^{\gamma} > 10$  GeV cut, for given input values of  $m_{\tilde{\chi}_1^{\pm}}$ ,  $\Delta m_{\tilde{\chi}}$  and  $c\tau$ . We decay the  $\tilde{\chi}_1^{\pm}$  according to the chosen  $c\tau$ , accounting for time-dilation for a given  $\tilde{\chi}_1^{\pm}$  velocity on an event-by-event basis. We compute the  $b_T$  of the final state  $\pi$ 's if they pass through the toy-model vertex detector as specified in [11], which includes a first (L00-like) layer at 1.6 cm. If  $b_T$  is  $\geq 5\sigma_b$ , where  $\sigma_b$  is the  $p_T^{\pi}$ -dependent impact parameter resolution given in [11], then we enter  $b_T$

<sup>3</sup>Even though the exact location of the event vertex using the  $\gamma$  trigger photon may be somewhat uncertain,  $b_T$  can be reliably measured as the distance in the transverse plane by which the projected  $\hat{p}_{\pi}$  unit vector misses the  $z$  axis.

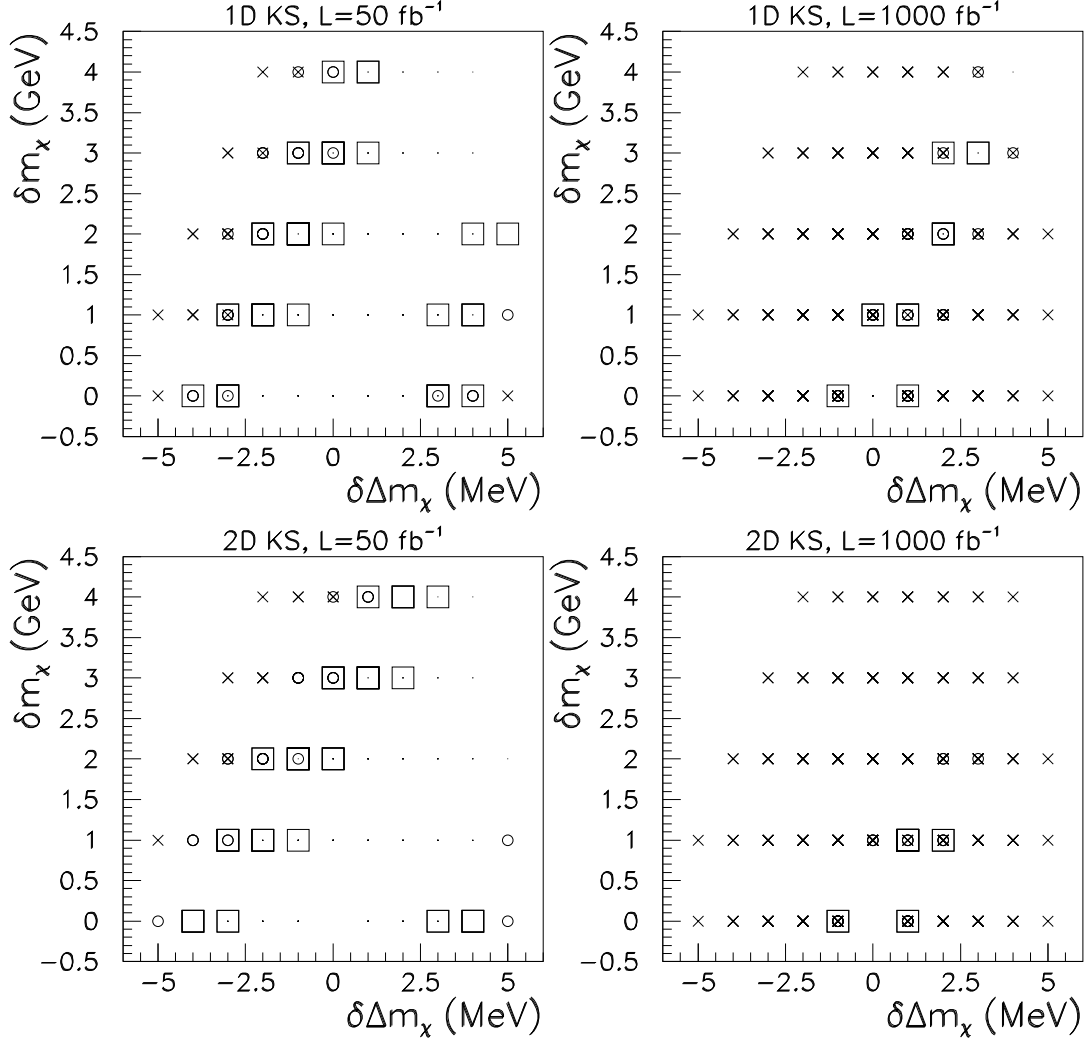


Figure 6: We show different levels of  $Q_{KS}^{1D}$  and  $Q_{KS}^{2D}$  computed from the  $E_\pi^*$  and  $[M_{\chi\chi}, E_\pi^*]$  distributions (respectively) for two different choices,  $A$  and  $B$ , of  $m_{\tilde{\chi}_1^\pm}$  and  $\Delta m_{\tilde{\chi}}$ , with  $173 < m_{\tilde{\chi}_1^\pm} < 177$  GeV and  $198 < \Delta m_{\tilde{\chi}} < 203$  MeV, as a function of  $\delta m_{\tilde{\chi}_1^\pm} \equiv m_{\tilde{\chi}_1^\pm}(A) - m_{\tilde{\chi}_1^\pm}(B)$  in GeV (taken to be  $> 0$  by convention) and  $\delta \Delta m_{\tilde{\chi}} \equiv \Delta m_{\tilde{\chi}}(A) - \Delta m_{\tilde{\chi}}(B)$  in MeV. Results shown are for  $L = 50 \text{ fb}^{-1}$  and  $L = 1 \text{ ab}^{-1}$ . The symbols  $\times$ ,  $\circ$ , and  $\square$  correspond to  $Q_{KS} < 0.1$ ,  $0.1 < Q_{KS} < 0.3$ , and  $0.3 < Q_{KS} < 0.68$ , respectively. Overlap of symbols means that different results are obtained for different choices of  $m_{\tilde{\chi}_1^\pm}(A)$  within the above range. Tiny dots are points that cannot be distinguished, while the blank locations were not sampled in our analysis.

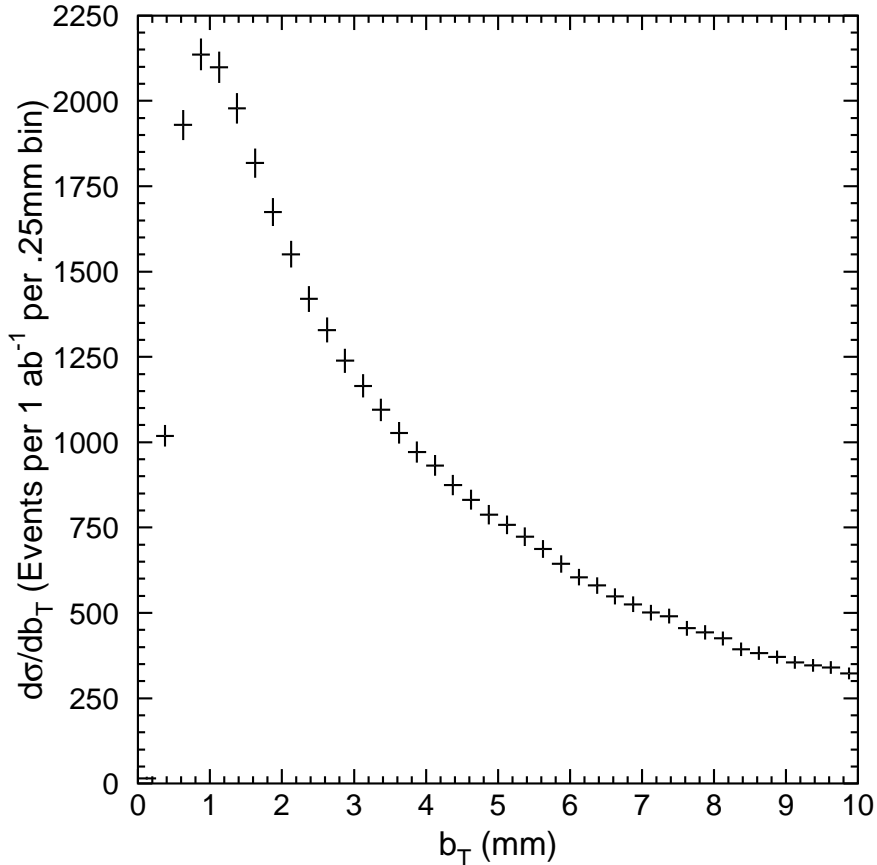


Figure 7: For  $\sqrt{s} = 600$  GeV,  $m_{\tilde{\chi}_1^\pm} = 175$  GeV,  $\Delta m_{\tilde{\chi}} = 200$  MeV and  $c\tau = 23.81$  mm, we plot the  $b_T$  distribution for the final  $\pi^\pm$  in  $e^+e^- \rightarrow \gamma\tilde{\chi}_1^+\tilde{\chi}_1^-$  after the cuts described in the text. The errors shown are those for  $L = 1$   $\text{ab}^{-1}$  of integrated luminosity.

in the appropriate impact parameter distribution bin. (There can be up to two entries per event.) The resulting distribution for  $m_{\tilde{\chi}_1^\pm} = 175$  GeV,  $\Delta m_{\tilde{\chi}} = 200$  MeV and  $c\tau = 23.81$  mm is plotted in Fig. 7. The bulk of the  $b_T$  distribution lies in the  $b_T < 10$  mm range. This is also the portion of the range for which fluctuations will be under control for bins of reasonable size. We have chosen a bin size of 0.25 mm and, in what follows, we will consider only the bins with  $b_T < 10$  mm. Because of the complicated kinematics (including the trigger photon), the limited size of the vertex detector, and the  $b_T \geq 5\sigma_b(p_T)$  requirement, the shape of the  $b_T$  distribution is not a simple exponential, and, in particular, is cutoff at low  $b_T$ . Assuming all these effects can be adequately modeled and studied via Monte Carlo, the  $b_T$  spectrum can provide considerable information regarding the underlying parameters. Indeed, the spectrum has a complicated dependence on  $m_{\tilde{\chi}_1^\pm}$  (as it affects the amount of  $\pi$  boost),  $\Delta m_{\tilde{\chi}}$  (as it affects the amount of momentum available for motion transverse to the  $\tilde{\chi}_1^\pm$  direction) and  $c\tau$ . Before the  $b_T \geq 5\sigma_b(p_T)$  requirement, the

$b_T$  distribution shifts to larger  $b_T$  with increasing  $c\tau$ , decreasing  $\Delta m_{\tilde{\chi}}$  and decreasing  $m_{\tilde{\chi}_1^\pm}$ . However, the  $b_T \geq 5\sigma_b(p_T)$  requirement removes more entries at low  $b_T$  for small  $\Delta m_{\tilde{\chi}}$  than for large  $\Delta m_{\tilde{\chi}}$ , with the result that larger  $\Delta m_{\tilde{\chi}}$  actually has more weight at small  $b_T$  than smaller  $\Delta m_{\tilde{\chi}}$ . We now summarize the ability to use the  $b_T$  distribution to determine  $c\tau$  and  $\Delta m_{\tilde{\chi}}$  for our detector model. We reemphasize that use of this technique requires that the acceptance and resolution of the vertex detector and the influence of the precise cuts made all be well understood.

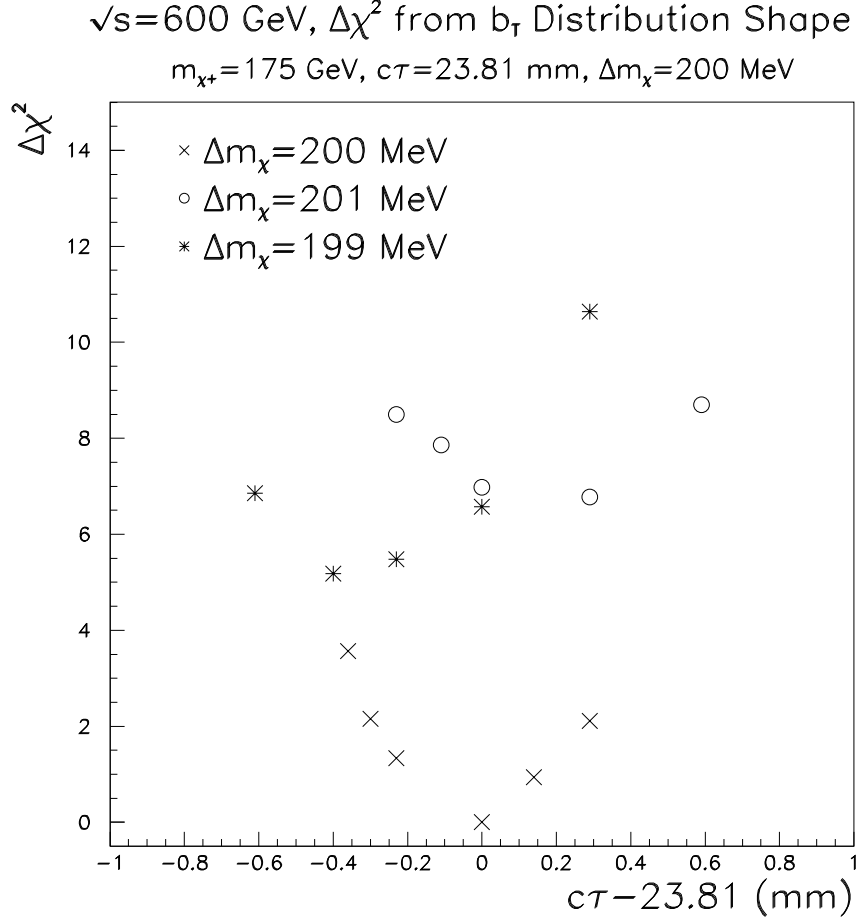


Figure 8: For  $m_{\tilde{\chi}_1^\pm} = 175$  GeV,  $\sqrt{s} = 600$  GeV and central values of  $\Delta m_{\tilde{\chi}} = 200$  MeV and  $c\tau = 23.81$  mm, we plot the  $\Delta\chi^2$  computed as a function of  $c\tau - 23.81$  mm for  $\Delta m_{\tilde{\chi}} = 199, 200$  and  $201$  MeV. We have assumed  $L = 1$   $\text{ab}^{-1}$ , and have chosen the relative normalization of the alternative distribution for each alternative parameter set so as to minimize  $\Delta\chi^2$ .

To be quantitative, we have proceeded as follows. We have chosen the central values of  $\Delta m_{\tilde{\chi}} = 200$  MeV,  $c\tau = 23.81$  mm and  $m_{\tilde{\chi}_1^\pm} = 175$  GeV. We then consider various neighboring values and compute the  $\Delta\chi^2$  between the  $b_T$  distribution for any given set of  $[\Delta m_{\tilde{\chi}}, c\tau, m_{\tilde{\chi}_1^\pm}]$  values and the central values using bins of size 0.25 mm in the region  $b_T \leq 10$  mm and choosing the relative normalization that minimizes  $\Delta\chi^2$ .

(i.e. we rely on shape differences only). The  $b_T$  distribution is insensitive to changes in  $m_{\tilde{\chi}_1^\pm}$  within the error of  $\pm 0.2$  GeV from the kinematic distribution techniques. Thus, it is most relevant to assess our ability to determine  $c\tau$  and  $\Delta m_{\tilde{\chi}}$  from the  $b_T$  distribution. Holding  $m_{\tilde{\chi}_1^\pm} = 175$  GeV fixed, the  $\Delta\chi^2$  values as a function of  $c\tau - 23.81$  mm are plotted for  $\Delta m_{\tilde{\chi}} = 199, 200$  and  $201$  MeV in Fig. 8. For two parameters, the  $1\sigma$  (68.27% CL) and  $2\sigma$  (95.45% CL)  $\Delta\chi^2$  values are 2.30 and 4.61. We see that, assuming  $L = 1 \text{ ab}^{-1}$ , a  $\Delta\chi^2$  value below 4.61 can only be achieved for  $\Delta m_{\tilde{\chi}}$  values within  $< 1$  MeV from  $\Delta m_{\tilde{\chi}} = 200$  MeV. Further, it is apparent that  $c\tau$  will be determined to better than  $\delta c\tau \sim 0.4$  mm at the  $1\sigma$  level, corresponding roughly to a  $\pm 2\%$  measurement of  $c\tau$ .

It is perhaps useful to see what features of the  $b_T$  distribution allow such precise parameter determination. To this end, we plot in Fig. 9 the differences,  $\Delta N$ , in the number of entries in a given  $b_T$  bin between the distributions for the central [ $\Delta m_{\tilde{\chi}} = 200$  MeV,  $c\tau = 23.81$  mm] parameter choice and those for [ $\Delta m_{\tilde{\chi}} = 201$  MeV,  $c\tau = 24.11$  mm] and [ $\Delta m_{\tilde{\chi}} = 199$  MeV,  $c\tau = 23.41$  mm]. The  $c\tau$  choices for these latter two  $\Delta m_{\tilde{\chi}}$  values are those which minimize the  $\Delta\chi^2$ , as shown in Fig. 8. The  $\Delta N$  values are those obtained after choosing the relative normalizations of the alternative parameter distributions so as to minimize the  $\Delta\chi^2$ . Also shown are the errors for a total luminosity of  $L = 1 \text{ ab}^{-1}$ . We observe a systematic variation, especially at low  $b_T$ , of the  $\Delta m_{\tilde{\chi}} = 201$  MeV and  $\Delta m_{\tilde{\chi}} = 199$  MeV distributions relative to that for  $\Delta m_{\tilde{\chi}} = 200$  MeV. There are a large number of bins, each with  $\Delta\chi^2 \gtrsim 0.5$ , which combine to give the significant overall  $\Delta\chi^2$  plotted in Fig. 8. (We have checked that these differences between the distributions are not an artifact of the Monte Carlo simulation statistics.) Note for instance the depletion in the smallest  $b_T$  bin for  $\Delta m_{\tilde{\chi}} = 201$  MeV, mentioned earlier, followed rapidly by an excess in the next set of  $b_T$  bins. We hope that these distributions make it apparent that both can be distinguished at a good level from that for [ $\Delta m_{\tilde{\chi}} = 200$  MeV,  $c\tau = 23.81$  mm] and that the distributions for the two alternative parameter choices can also be clearly distinguished from one another.

In the above analysis, we have implicitly assumed that there are no contaminating background events. After our minimal  $p_T^\gamma > 10$  GeV tag cut, backgrounds (including the two-photon backgrounds) are unlikely to yield events having significant impact parameters.<sup>4</sup>

A measurement of  $c\tau$  can be converted to a joint constraint on  $\Delta m_{\tilde{\chi}}$  and the underlying  $M_1, M_2, \mu, \tan\beta$  parameters. Consider  $\Delta m_{\tilde{\chi}} < 700$  MeV for which the only modes of any importance are  $\tilde{\chi}_1^\pm \rightarrow \ell^\pm \nu \tilde{\chi}_1^0$  and  $\tilde{\chi}_1^\pm \rightarrow \pi^\pm \tilde{\chi}_1^0$ . For the latter, we have

$$\Gamma(\tilde{\chi}_1^- \rightarrow \tilde{\chi}_1^0 \pi^-) = \frac{f_\pi^2 G_F^2 |\vec{k}_\pi|}{4\pi m_{\tilde{\chi}_1^\pm}^2} \left\{ \left( O_{11}^L + O_{11}^R \right)^2 \left[ \left( m_{\tilde{\chi}_1^\pm}^2 - m_{\tilde{\chi}_1^0}^2 \right)^2 - m_\pi^2 \left( m_{\tilde{\chi}_1^\pm} - m_{\tilde{\chi}_1^0} \right)^2 \right] \right. \\ \left. + \left( O_{11}^L - O_{11}^R \right)^2 \left[ \left( m_{\tilde{\chi}_1^\pm}^2 - m_{\tilde{\chi}_1^0}^2 \right)^2 - m_\pi^2 \left( m_{\tilde{\chi}_1^\pm} + m_{\tilde{\chi}_1^0} \right)^2 \right] \right\}, \quad (7)$$

where the  $O_{11}^{L,R}$  describe the  $W^\mp \tilde{\chi}_1^\pm \tilde{\chi}_1^0$  coupling,

$$O_{11}^L = -\frac{1}{\sqrt{2}} N_{14} V_{12} + N_{12} V_{11}, \quad O_{11}^R = +\frac{1}{\sqrt{2}} N_{13} U_{12} + N_{12} U_{11}. \quad (8)$$

---

<sup>4</sup>If  $c\tau$  is of the order of  $100 \mu\text{m}$ , then a precise accounting for the  $e^+e^- \rightarrow e^+e^- \gamma \tau^+ \tau^- \rightarrow \gamma \pi^+ \pi^- E$  background might be necessary.

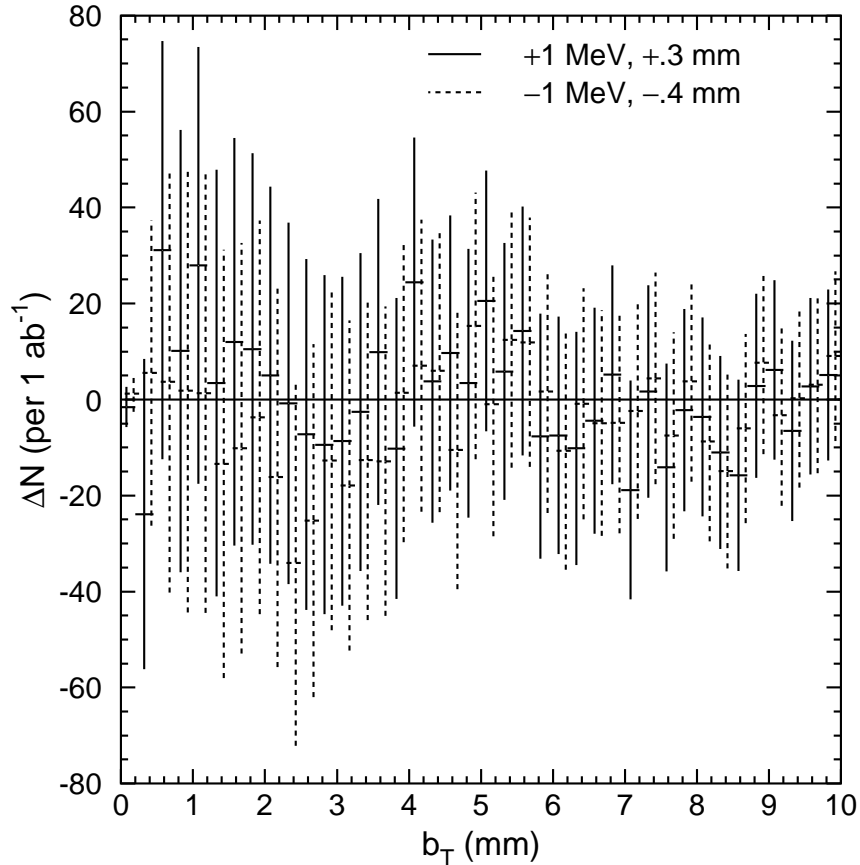


Figure 9: For  $m_{\tilde{\chi}_1^\pm} = 175$  GeV and  $\sqrt{s} = 600$  GeV, we plot the differences,  $\Delta N$ , (of the number of entries in a given bin) between the  $b_T$  spectra for the central values of  $[\Delta m_{\tilde{\chi}} = 200$  MeV,  $c\tau = 23.81$  mm] and those for  $[\Delta m_{\tilde{\chi}} = 201$  MeV,  $c\tau = 24.11$  mm] and  $[\Delta m_{\tilde{\chi}} = 199$  MeV,  $c\tau = 23.41$  mm]. These differences plotted are those found after choosing the normalizations of the distributions for the latter two alternative parameter choices so as to minimize  $\Delta\chi^2$ . Also shown are the errors for a total luminosity of  $L = 1$   $\text{ab}^{-1}$ . We have artificially shifted the  $b_T$  values at which the points are plotted so that the two different cases can be distinguished.

Current experiment gives  $f_\pi = 92.42 \pm 0.3$  MeV, which yields a  $\sim 0.7\%$  error for this width. More important is the parameter dependence of  $O_{11}^{L,R}$ . Naively, these are  $\sim 1$  for the wino-like LSP scenario. However, their dependence on the underlying SUSY parameters  $M_1, M_2, \mu, \tan\beta$  is significant. For example, for  $m_{\tilde{\chi}_1^\pm} \sim 175$  GeV, they vary by about 5% as  $|\mu|$  increases in the range 500 GeV to 1 TeV, with much more dramatic variation as  $|\mu|$  approaches 300 GeV. At large  $|\mu| > 500$  GeV the  $O_{11}^{L,R}$  also vary by about (1 – 2)% as  $\tan\beta$  ranges from small to large values. At smaller  $|\mu|$ , the  $\tan\beta$  variation is much more dramatic. The widths for the  $\tilde{\chi}_1^\pm \rightarrow \ell^\pm \nu \tilde{\chi}_1^0$  ( $\ell = e, \mu$ ) modes are also proportional to combinations of the

$O_{11}^{L,R}$ . If the  $O_{11}^{L,R}$  are held fixed at the Ref. [2] central values, Eq. (7) implies that a shift in  $\Delta m_{\tilde{\chi}}$  by 1 MeV corresponds (in the vicinity of  $\Delta m_{\tilde{\chi}} \sim 200$  MeV) to a shift in  $c\tau$  by about 2.5%. However, there are many parameter choices that yield the same  $\Delta m_{\tilde{\chi}}$  with  $O_{11}^{L,R}$  values that differ by more than this. Given these uncertainties and the  $\sim 2\%$  experimental error for the  $c\tau$  determination, it will be difficult to constrain  $\Delta m_{\tilde{\chi}}$  more accurately than via the experimentally direct kinematic distribution and  $b_T$  shape fit techniques. Ultimately, the reverse strategy might prove useful. That is, determine  $\Delta m_{\tilde{\chi}}$  directly from the kinematic distributions and  $b_T$  distribution shape and  $c\tau$  from the  $b_T$  distribution shape and then use these values to constrain the  $M_1, M_2, \mu, \tan\beta$  parameters. Note that it would be crucial to include the one-loop corrections to  $\Delta m_{\tilde{\chi}}$  in this process.

**5. Determining  $M_2$ ,  $\mu$  and  $\tan\beta$ .** Let us suppose that we have accurate determinations of  $m_{\tilde{\chi}_1^\pm}$  and  $\Delta m_{\tilde{\chi}}$  using the kinematic distribution techniques described above. We will then wish to extract the underlying SUSY parameters. We study our ability to do so for the specific case of  $m_{\tilde{\chi}_1^\pm} = 175$  GeV and  $\Delta m_{\tilde{\chi}} = 200$  MeV. This particular case is motivated in the context of ( $\delta_{GS} = 0$  O-II)/AMSB one-loop boundary conditions: (a)  $m_{\tilde{\chi}_1^\pm} < 200$  GeV is preferred if we are to avoid the extreme fine-tuning for larger  $m_{\tilde{\chi}_1^\pm}$  implied by the large value ( $\sim 10$ ) predicted for  $M_3/M_2$ ; and (b)  $\Delta m_{\tilde{\chi}} < 200 - 500$  MeV is preferred because of the large value predicted for  $M_1/M_2$ . We again remind the reader that, for such  $\Delta m_{\tilde{\chi}}$ , the  $\gamma\tilde{\chi}_1^+\tilde{\chi}_1^-$  events we employ will be background free since at least one of the final  $\pi$ 's will have an observable HIP.

The SUSY parameters entering into the chargino sector at tree level are  $M_2, \mu$  and  $\tan\beta$ . The measured value of  $m_{\tilde{\chi}_1^\pm}$  provides only one constraint on these three parameters. The projection of this constraint on the standard  $[\mu, M_2]$  plane gives the two regions indicated in Fig. 10 by the outer solid lines. In this paper, we restrict ourselves to  $|\mu| > 300$  GeV, since for lower  $|\mu|$  the  $\tilde{\chi}_2^\pm$  charginos would also be produced and the nature of the analysis and parameter extraction procedures would change dramatically. Typical radiative electroweak symmetry breaking favors large  $|\mu|$  values.

The goal is to use the  $\gamma\tilde{\chi}_1^+\tilde{\chi}_1^-$  production cross section and kinematic dependencies to obtain additional constraints on the three parameters. Sensitivity to these parameters arises entirely through the coupling of the  $Z$  to  $\tilde{\chi}_1^+\tilde{\chi}_1^-$ :

$$\frac{ig}{c_W}\gamma^\mu \left( O_{11}^{\prime L} P_L + O_{11}^{\prime R} P_R \right), \quad \text{with } O_{11}^{\prime L} = -c_W^2 + \frac{1}{2}V_{12}^2, \quad O_{11}^{\prime R} = -c_W^2 + \frac{1}{2}U_{12}^2, \quad (9)$$

where  $c_W \equiv \cos\theta_W$  etc., and  $V_{12}$  and  $U_{12}$  are elements of the matrices that diagonalize the chargino mass matrix. (In our work, we neglect possible CP-violating phases in the chargino sector.) Their squares can be written in the form  $V_{12}^2 = \frac{1}{2}(1 - \cos 2\phi_L)$  and  $U_{12}^2 = \frac{1}{2}(1 - \cos 2\phi_R)$  with

$$\begin{aligned} \cos 2\phi_L &= -\frac{M_2^2 - \mu^2 - 2m_W^2 \cos 2\beta}{\sqrt{(M_2^2 + \mu^2 + 2m_W^2)^2 - 4(M_2\mu - m_W^2 \sin 2\beta)^2}}, \\ \cos 2\phi_R &= -\frac{M_2^2 - \mu^2 + 2m_W^2 \cos 2\beta}{\sqrt{(M_2^2 + \mu^2 + 2m_W^2)^2 - 4(M_2\mu - m_W^2 \sin 2\beta)^2}}. \end{aligned} \quad (10)$$

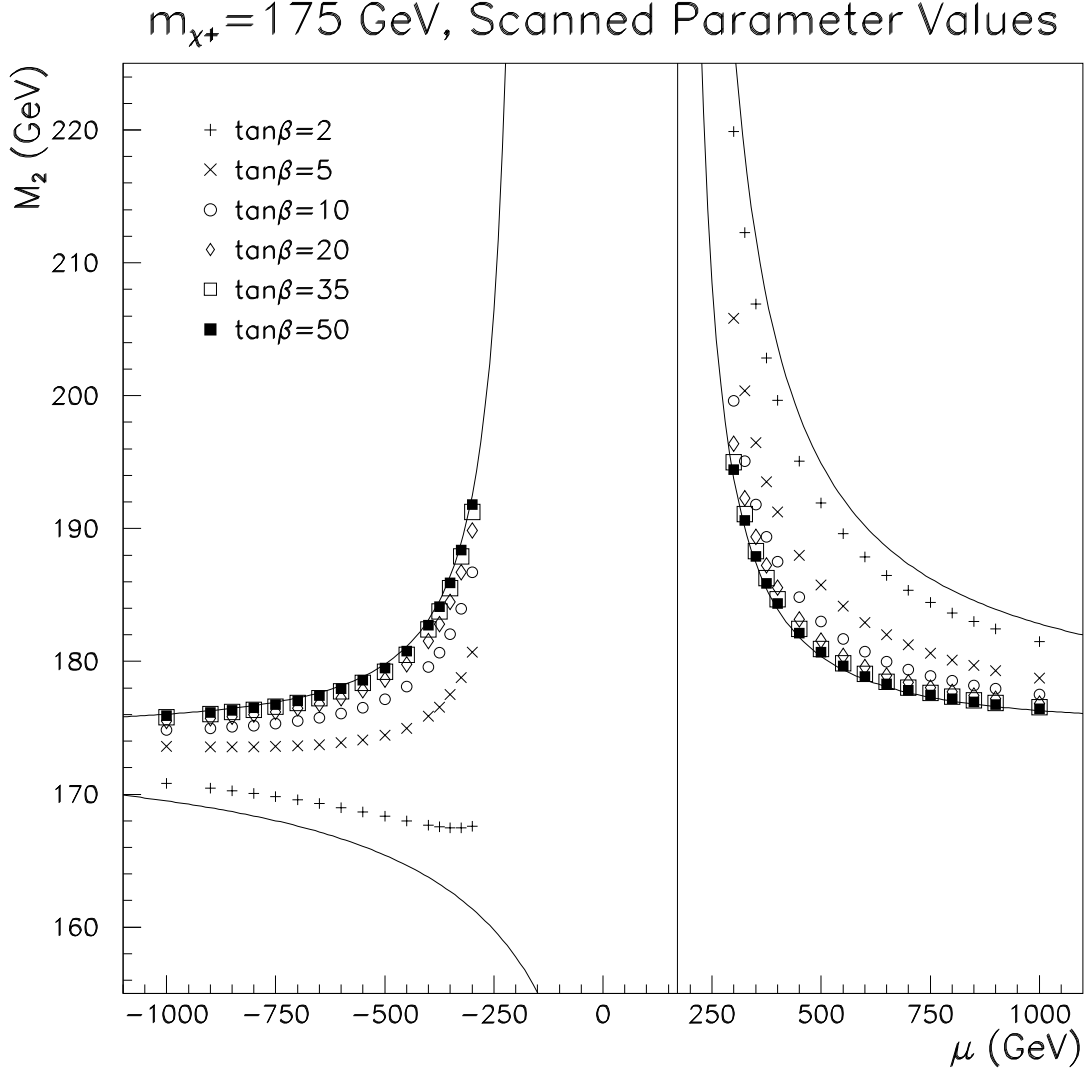


Figure 10: For  $m_{\tilde{\chi}_1^\pm} = 175$  GeV, the outer solid lines show the region in the  $[\mu, M_2]$  plane consistent with  $1 \leq \tan \beta \leq 100$  and  $|\mu| > 150$  GeV. Also shown are the values of  $[\mu, M_2]$  sampled for  $\tan \beta = 2, 5, 10, 20, 35, 50$  in determining our fits to the  $e^+e^- \rightarrow \gamma \tilde{\chi}_1^+ \tilde{\chi}_1^-$  cross sections.

Asymptotic expressions for  $V_{12}$  and  $U_{12}$ , valid for  $|M_2 \pm \mu| \gg m_Z$  are [21] (using  $c_\beta \equiv \cos \beta$  etc.):

$$V_{12} = \frac{m_W \sqrt{2} (M_2 s_\beta + \mu c_\beta)}{M_2^2 - \mu^2}, \quad U_{12} = \frac{m_W \sqrt{2} (M_2 c_\beta + \mu s_\beta)}{M_2^2 - \mu^2}. \quad (11)$$

Clearly  $V_{12}^2$  and  $U_{12}^2$  are small compared to  $c_W^2$  when  $|\mu|$  is large. Further,  $U_{12}^2 \gg V_{12}^2$  is typical for  $\tan \beta > 2$  when  $|\mu| \gg M_2$ . In the scenarios we consider, the  $\tilde{\chi}_1^\pm$  are indeed highly wino-like and, thus, the problem is to pick out the small  $V_{12}^2$  and  $U_{12}^2$  corrections to the dominant  $-c_W^2$  term in the  $Z$  coupling.



To understand how to proceed, it is useful to first briefly review results for  $e^+e^- \rightarrow \tilde{\chi}_1^+ \tilde{\chi}_1^-$  without a photon tag. Following [22], we write

$$T(e^+e^- \rightarrow \tilde{\chi}_1^+ \tilde{\chi}_1^-) = \frac{e^2}{s} \sum_{\alpha, \beta=R,L} Q_{\alpha\beta}(s) [\bar{v}(e^+) \gamma_\mu P_\alpha u(e^-)] [\bar{u}(\tilde{\chi}_1^-) \gamma^\mu P_\beta v(\tilde{\chi}_1^+)] \quad (12)$$

where

$$\begin{aligned} Q_{LL}(s) &= 1 + \frac{D_Z(s)}{s_W^2 c_W^2} (s_W^2 - \frac{1}{2}) \left( -c_W^2 + \frac{1}{2} V_{12}^2 \right), \\ Q_{LR}(s) &= 1 + \frac{D_Z(s)}{s_W^2 c_W^2} (s_W^2 - \frac{1}{2}) \left( -c_W^2 + \frac{1}{2} U_{12}^2 \right) + \frac{D_{\tilde{\nu}}(s, t)}{4s_W^2} (2 - U_{12}^2), \\ Q_{RL}(s) &= 1 + \frac{D_Z(s)}{c_W^2} \left( -c_W^2 + \frac{1}{2} V_{12}^2 \right), \\ Q_{RR}(s) &= 1 + \frac{D_Z(s)}{c_W^2} \left( -c_W^2 + \frac{1}{2} U_{12}^2 \right), \end{aligned}$$

In Eq. (13),  $D_Z(s) = s/(s - m_Z^2)$  and  $D_{\tilde{\nu}}(s, t) = s/(t - m_{\tilde{\nu}}^2)$ . It is crucial to observe that  $Q_{RL} \sim \frac{1}{2c_W^2} V_{12}^2$  and  $Q_{RR} \sim \frac{1}{2c_W^2} U_{12}^2$  at large  $s$ , implying that a right-handed polarized  $e^-$  beam will provide a very direct probe of  $V_{12}^2$  and  $U_{12}^2$ , but at the sacrifice of a very suppressed cross section. Pure  $e_R^-$  also has the advantage of eliminating the ‘background’ from the  $\tilde{\nu}_e$  exchange diagram. Since this diagram will significantly suppress the unpolarized cross section for  $m_{\tilde{\nu}_e} < 1$  TeV (i.e. even for masses for which we will not be able to directly detect the  $\tilde{\nu}_e$  and measure its mass), the normalization of the unpolarized cross section cannot be calculated reliably enough to use as an ingredient in extracting the parameters of the model. The importance of the polarized measurements, for which this is not a problem, implies that maximal integrated luminosity will thus be of paramount importance, whether one is looking at an mSUGRA-type SUSY breaking scenario or, as we shall discuss in detail shortly, the degenerate  $m_{\tilde{\chi}_1^\pm} \sim m_{\tilde{\chi}_1^0}$  scenario. In terms of the  $Q_{\alpha\beta}$ ’s, the  $e^+e^- \rightarrow \tilde{\chi}_1^+ \tilde{\chi}_1^-$  amplitude squared is

$$|\mathcal{A}|^2 \propto (-2\vec{p}_{\tilde{\chi}_1^-} \cdot p_{e^-} \vec{p}_{\tilde{\chi}_1^+} \cdot p_{e^+} s(Q_{LR}^2 + Q_{RL}^2) - 2\vec{p}_{\tilde{\chi}_1^-} \cdot p_{e^+} \vec{p}_{\tilde{\chi}_1^+} \cdot p_{e^-} s(Q_{LL}^2 + Q_{RR}^2) - s^2 m_{\tilde{\chi}_1^\pm}^2 (Q_{LL} Q_{LR} + Q_{RL} Q_{RR}))/2 \quad (13)$$

where  $p_{\tilde{\chi}_1^-} \cdot p_{e^-} = p_{\tilde{\chi}_1^+} \cdot p_{e^+} \simeq E_b^2 (1 - \beta \cos \theta)$ ,  $p_{\tilde{\chi}_1^-} \cdot p_{e^+} = p_{\tilde{\chi}_1^+} \cdot p_{e^-} \simeq E_b^2 (1 + \beta \cos \theta)$ ,  $\beta^2 = 1 - m_{\tilde{\chi}_1^\pm}^2/E_b^2$  and  $E_b = \sqrt{s}/2$ . By measuring the magnitude of the cross section, especially for a right-handed polarized  $e^-$  beam, and its dependence on  $\cos \theta$ , one can hope to determine the charges  $Q_{\alpha\beta}$  and, thence, the crucial  $V_{12}^2$  and  $U_{12}^2$  matrix entries that probe  $\mu$ ,  $M_2$  and  $\tan \beta$ . The  $\tilde{\chi}_1^\pm$  are not directly observed (unless they have a substantial path length, as is possible in this model but not assumed in our analysis), but, by using the accurately measured values of  $m_{\tilde{\chi}_1^\pm}$  and  $\Delta m_{\tilde{\chi}}$  and the measured three-momenta of the  $\pi^\pm$ , the chargino momenta can be reconstructed up to a two-fold ambiguity. The analogue of this reconstruction for the  $\gamma \tilde{\chi}_1^+ \tilde{\chi}_1^-$  final state is discussed in the Appendix. We note that  $|\mathcal{A}|^2$  and, thence, the integrated cross section for any particular machine energy and set of cuts depend bi-quadratically on  $V_{12}^2$  and  $U_{12}^2$ .

These same ‘charges’,  $Q_{\alpha\beta}$ , appear in the expression for the  $e^+e^- \rightarrow \gamma \tilde{\chi}_1^+ \tilde{\chi}_1^-$  amplitude, which contains two initial state radiation diagrams summed over  $Q_{\alpha\beta}(q^2 = M_{\chi\chi}^2)$ ’s and two final state radiation diagrams summed over  $Q_{\alpha\beta}(q^2 = s)$ ’s, where  $q$  is the four-momentum carried by the virtual  $Z$  or  $\gamma$ . The resulting

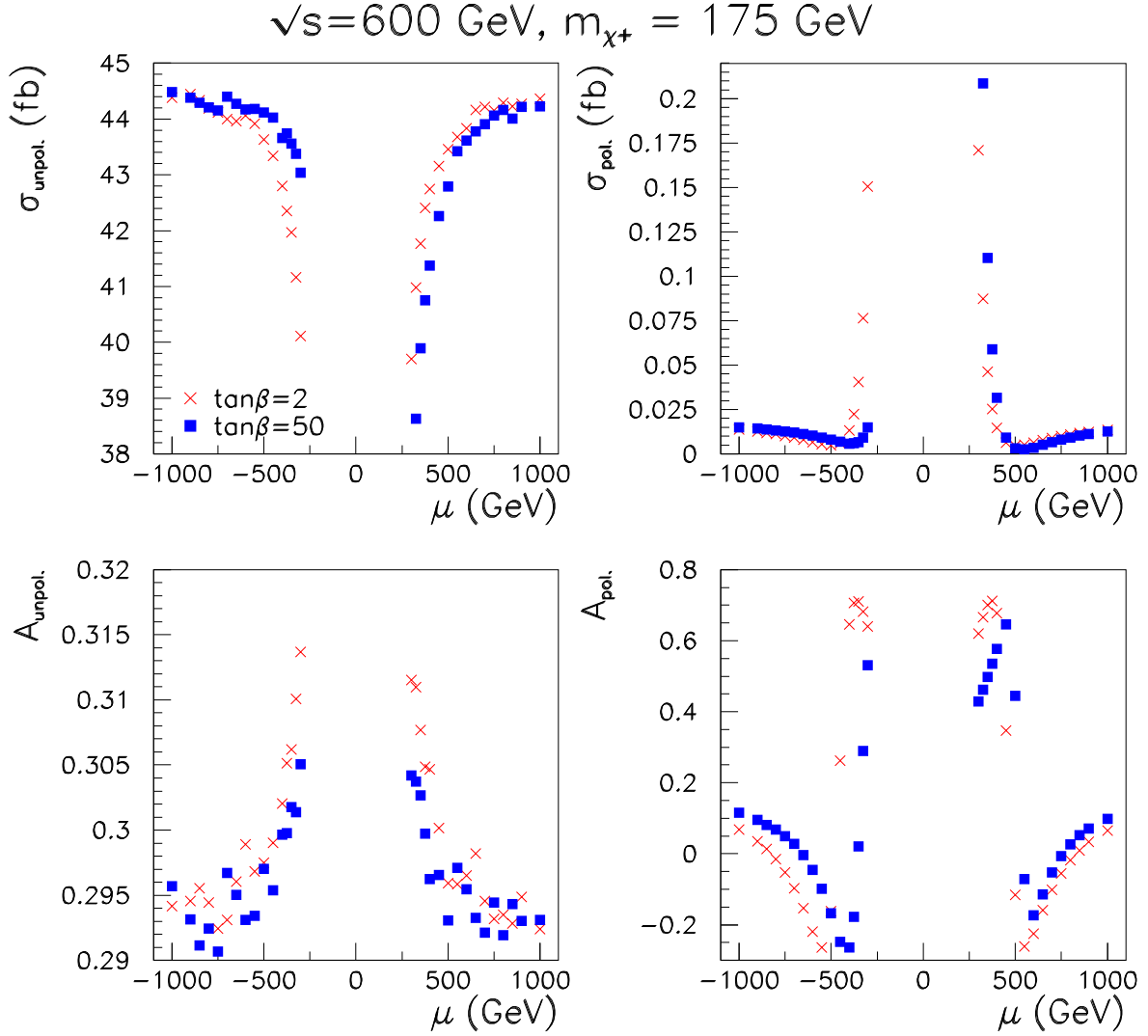


Figure 11: For  $m_{\tilde{\chi}_1^\pm} = 175 \text{ GeV}$ , we plot  $\sigma$  and  $A$  as a function of  $\mu$  for  $\tan\beta = 2$  and 50. Results are given for an unpolarized  $e^-$  beam and a purely  $e_R^-$  beam at  $\sqrt{s} = 600 \text{ GeV}$ . A mass splitting of  $\Delta m_{\tilde{\chi}} = 200 \text{ MeV}$  was employed in generating the  $\pi^\pm$  momenta.

form for  $|\mathcal{A}|^2$  has a complicated dependence on many kinematical variables. (In the Appendix, we give the structure of  $|\mathcal{A}|^2$  for the dominant initial state radiation diagrams. An expression in a different formalism for the full  $|\mathcal{A}|^2$  is given in [15].) In the soft-photon limit,  $|\mathcal{A}(e^+e^- \rightarrow \gamma\tilde{\chi}_1^+\tilde{\chi}_1^-)|^2$  is directly proportional to  $|\mathcal{A}(e^+e^- \rightarrow \tilde{\chi}_1^+\tilde{\chi}_1^-)|^2$ , but this limit does not allow an understanding of all of the features of the  $\gamma\tilde{\chi}_1^+\tilde{\chi}_1^-$  cross section. However, it remains true that right handed electron polarization produces a very suppressed cross section with high sensitivity to  $V_{12}^2$  and  $U_{12}^2$  and no sensitivity to the probably unknown  $\tilde{\nu}_e$  mass.

We now outline our precise procedures. For each event, the observed  $\gamma$  defines a chargino-pair, i.e.  $M_{\chi\chi}$ , center of mass system. In this c.m.s., we have followed the Collins-Soper procedure [23] of defining a  $z$ -axis by boosting along the  $\gamma$  direction to the  $M_{\chi\chi}$  c.m.s., determining the unit vectors  $\hat{u}_{e^\pm}$  in the  $e^\pm$  three momentum directions after the boost and defining  $\hat{z} = (\hat{u}_{e^+} - \hat{u}_{e^-}) / (2 - 2\hat{u}_{e^+} \cdot \hat{u}_{e^-})$ . For the vast majority of events,  $\hat{z}$  is very closely aligned with the  $z$  axis in the laboratory frame. We then determine the  $\tilde{\chi}_1^\pm$  momenta in this frame (using the observed  $\pi^\pm$  momenta and the known values of  $m_{\tilde{\chi}_1^\pm}$  and  $m_{\tilde{\chi}_1^0} = m_{\tilde{\chi}_1^\pm} - \Delta m_{\tilde{\chi}}$ ) following the procedure of the Appendix and compute the angle,  $\hat{\theta}$ , of  $\vec{p}_{\tilde{\chi}_1^-}$  with respect to  $\hat{z}$ . ( $\vec{p}_{\tilde{\chi}_1^+} = -\vec{p}_{\tilde{\chi}_1^-}$  in the  $M_{\chi\chi}$  c.m.s.) Since there is a two-fold ambiguity in the reconstruction, we bin events twice corresponding to the two possible reconstructed  $\tilde{\chi}_1^\pm$  three-momenta.

We have restricted our analysis to the absolute magnitude of the cross section,  $\sigma$ , and the asymmetry

$$A \equiv \frac{\sigma(\cos \hat{\theta} > 0) - \sigma(\cos \hat{\theta} < 0)}{\sigma(\cos \hat{\theta} > 0) + \sigma(\cos \hat{\theta} < 0)} \quad (14)$$

where the cross sections are obtained by integrating over all of phase space consistent with the specified sign of  $\cos \hat{\theta}$  and our basic  $p_T^\gamma > 10$  GeV and  $10^\circ < \theta_\gamma < 170^\circ$  photon-tag cuts. We illustrate the dependence of  $\sigma$  and  $A$  on  $\mu$  for  $\tan \beta = 2$  and 50 in Fig. 11. ( $M_2$  is determined as a function of  $\mu$  at a given  $\tan \beta$  by the fixed value of  $m_{\tilde{\chi}_1^\pm} = 175$  GeV as shown in Fig. 10.) Results are given for unpolarized beams and for the case of a purely right-handed polarized electron beam. For  $L = 1 \text{ ab}^{-1}$ , typical  $1\sigma$  errors for  $\sigma$  and  $A$  are of order 0.5% and 1% (15% and 50%) for the unpolarized (polarized) cases, respectively. Relative to the above-quoted typical errors, there is significant variation with respect to  $\mu$  of both  $\sigma$  and  $A$ , but different  $\tan \beta$  values will be difficult to separate since a large change in  $\tan \beta$  can be compensated by a small shift in  $\mu$  that will leave the four observables more or less unchanged. The variations with  $\mu$  are especially dramatic for  $\sigma_{\text{polarized}}$  and  $A_{\text{polarized}}$ , but the large statistical errors even for  $L = 1 \text{ ab}^{-1}$  render these variations no more (or less) useful than those for the corresponding observables in the unpolarized beam case. Since the polarized and unpolarized cross sections and asymmetries contain different weightings of  $U_{12}^2$  and  $V_{12}^2$ , accumulating significant luminosity in both modes is useful for maximizing our ability to determine  $U_{12}^2$  and  $V_{12}^2$ .

	$a$	$b$	$c$	$d$	$e$	$f$
$\sigma_U^+$	28.7596	-5.48626	-15.5788	0.20296	1.07641	5.98101
$\sigma_U^-$	15.7698	-7.08801	-4.67496	0.0723394	-1.1899	4.98557
$\sigma_P^+$	0.0111671	-0.323629	-0.124093	2.91672	0.637143	1.26579
$\sigma_P^-$	0.00771917	-0.103494	-0.169943	0.59423	1.27397	0.784927

Table 6: Tabulation of fitted parameters  $a, b, c, d, e, f$  (in units of fb's) of Eq. (15) for each of the four cross sections employed in our analysis. Results are for  $\sqrt{s} = 600$  GeV and are those obtained after Monte Carlo integration incorporating cuts and the chargino reconstruction algorithm described.

To simplify our analysis, we scanned a large selection of  $\mu$  values in the ranges  $[-1000 \text{ GeV}, -300 \text{ GeV}]$

and [300 GeV, 1000 GeV] at a series of  $\tan\beta$  values ( $\tan\beta = 2, 5, 10, 20, 35, 50$ )<sup>5</sup> and fit the results for 1)  $\sigma_U^+ \equiv \sigma_{\text{unpolarized}}(\cos\hat{\theta} > 0)$ , 2)  $\sigma_U^- \equiv \sigma_{\text{unpolarized}}(\cos\hat{\theta} < 0)$ , 3)  $\sigma_P^+ \equiv \sigma_{\text{polarized}}(\cos\hat{\theta} > 0)$  and 4)  $\sigma_P^- \equiv \sigma_{\text{polarized}}(\cos\hat{\theta} < 0)$  to the bi-quadratic form (required by the amplitude structure)

$$\sigma_i = a + bU_{12}^2 + cV_{12}^2 + d(U_{12}^2)^2 + e(V_{12}^2)^2 + fU_{12}^2V_{12}^2. \quad (15)$$

Results for  $a - f$  for  $\sqrt{s} = 600$  GeV,  $m_{\tilde{\chi}_1^\pm} = 175$  GeV and  $\Delta m_{\tilde{\chi}} = 200$  MeV (the latter possibly affecting reconstruction of the angle of the chargino) are given in Table 6. These fits give the correct cross section with an accuracy of better than 0.7% for all the sampled points. For  $\sigma_P^+$  and  $\sigma_P^-$ , note the very small constant terms and the much larger quartic term coefficients ( $d, e, f$ ). As already discussed, this is to be expected and follows from the wino-like nature of the  $\tilde{\chi}_1^\pm$ .

We now employ these cross section fits to study the accuracy with which we can expect to determine  $M_2$ ,  $\mu$  and  $\tan\beta$ . To illustrate, we give in Fig. 12, for  $\sqrt{s} = 600$  GeV, contours of  $\Delta\chi^2 = 2.30$  (68% CL for two independent parameters) and  $\Delta\chi^2 = 13$  (99% CL), using reference models of  $[\tan\beta, \mu] = [5, 375 \text{ GeV}]$  and  $[5, 600 \text{ GeV}]$ . For this figure, we employ the following set of observables: the forward/backward asymmetry for unpolarized beams; the absolute cross section for polarized beams; and the forward/backward asymmetry for polarized beams.<sup>6</sup> As explained later, the absolute unpolarized cross section is likely to have systematic theoretical uncertainties that are much larger than the statistical errors, and is not employed. We observe that, at the 68% CL,  $M_2$  and  $|\mu|$  can be determined to  $\sim 8\%$  and  $\sim 16\%$ , respectively, for  $|\mu| \sim 400$  GeV and to  $\sim 8\%$  and  $\sim 40\%$ , respectively, for  $|\mu| \sim 600$  GeV;  $\tan\beta$  is essentially undetermined. The 68% CL limits on  $\mu$  and  $M_2$  for a wider selection of input  $\mu$  values and input  $\tan\beta$  values of 5 and 20 are shown in Fig. 13. Results for other  $\tan\beta$  values are quite similar. Unless  $\tan\beta$  has been determined by other data, we must combine all such graphs and take the outer errors. Clearly, at the highest  $|\mu|$  values, errors for the  $\mu$  and  $M_2$  determinations become quite large, and significant uncertainty in  $M_2$  develops as  $\mu$  falls below 300 GeV.

The unpolarized cross section can provide useful constraints on SUSY parameters only if systematic errors are substantially smaller than the typical 5%-10% variation of  $\sigma_{\text{unpolarized}}$  as a function of parameters; see Fig. 11. Systematic *experimental* errors at an electron collider should be quite small, probably even smaller than the  $\sim 0.5\%$  statistical errors. However, theoretical uncertainties in  $\sigma_{\text{unpolarized}}$  must also be well below the 5%-10% level. Even if we assume that the  $\tilde{\nu}_e$  contribution can be absolutely normalized (for example, using  $\tilde{\nu}_e$  observations from the LHC) higher-order electroweak corrections to the  $e^+e^- \rightarrow \gamma\tilde{\chi}_1^+\tilde{\chi}_1^-$  cross section will need to be computed. In addition, one will be implicitly assuming that the supersymmetric  $Z\tilde{\chi}_1^+\tilde{\chi}_1^-$  coupling strength is indeed precisely that predicted by assuming strict supersymmetry for tree-level couplings. This will be difficult to independently check. Finally, to employ the absolute normalization of the unpolarized cross section one would need to rely on the modeling employed for computing the  $\tilde{\chi}_1^\pm \rightarrow \pi^\pm\tilde{\chi}_1^0$  branching ratio at the  $\lesssim 5\%$  level. The computation for the  $\tilde{\chi}_1^\pm \rightarrow \ell^\pm\nu\tilde{\chi}_1^0$  and  $\tilde{\chi}_1^\pm \rightarrow \pi^\pm\tilde{\chi}_1^0$  widths was

<sup>5</sup>The value of  $M_2$  at each point is determined by  $m_{\tilde{\chi}_1^\pm}$ .

<sup>6</sup>We compute the error in  $A \equiv \frac{N^+ - N^-}{N}$  as  $\delta A = \sqrt{\frac{1 - A^2}{N}}$ , where  $N = N^+ + N^-$ .

$L=2\text{ab}^{-1}$  total,  $\sqrt{s}=600$  only,  $\sigma_{\text{unpol.}}$  excluded  
 $m_{\tilde{\chi}_1^\pm} = 175$  GeV

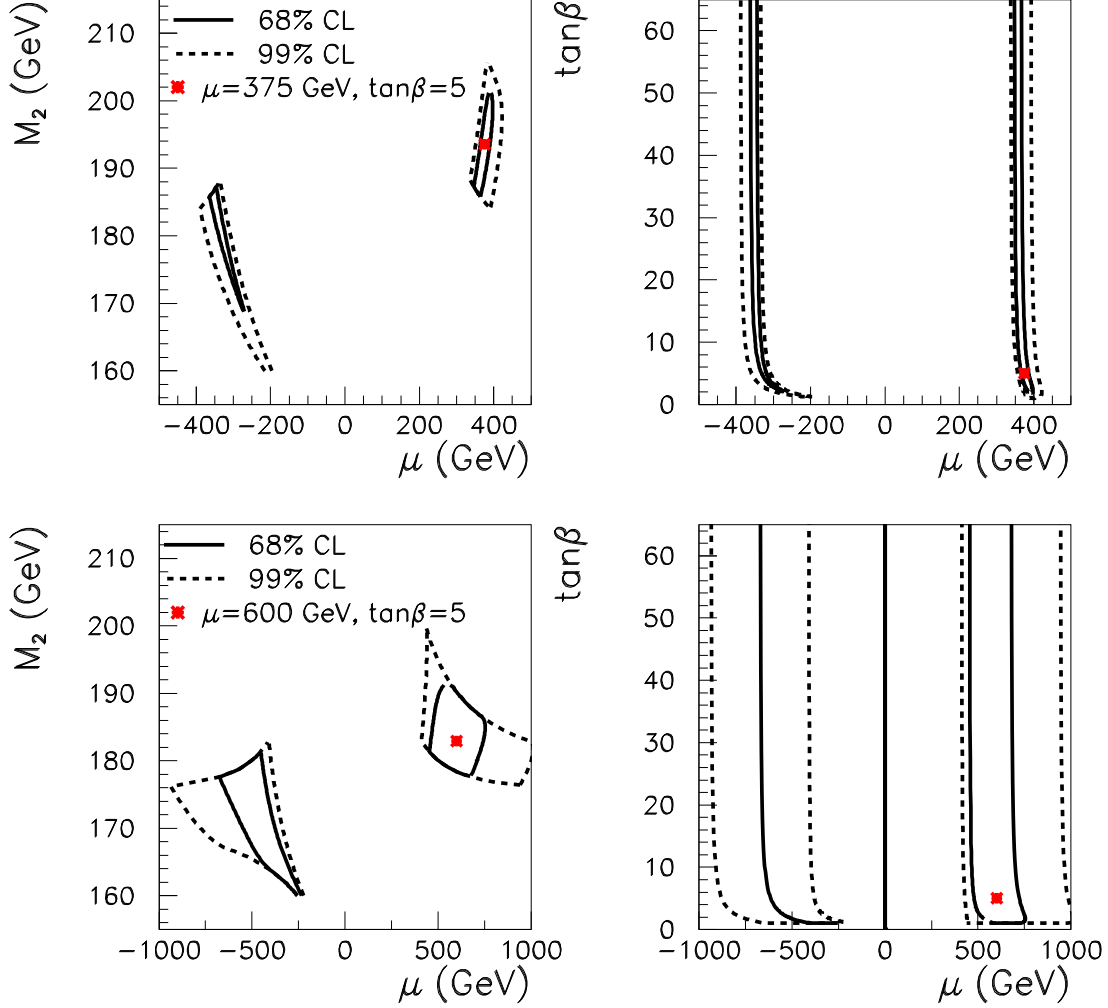


Figure 12: For  $m_{\tilde{\chi}_1^\pm} = 175$  GeV, we plot the contours for  $\Delta\chi^2 = 2.3$  (68% CL for two independent variables) and  $\Delta\chi^2 = 13$  (99% CL) in the  $[\mu, M_2]$  and  $[\mu, \tan\beta]$  parameter spaces using the two reference cases of  $[\tan\beta, \mu] = [5, 375 \text{ GeV}]$  and  $[5, 600 \text{ GeV}]$ . We have assumed running at  $\sqrt{s} = 600$  GeV sufficient to accumulate integrated luminosities of  $L = 1 \text{ ab}^{-1}$  for both unpolarized beams and for a purely right-handed electron beam. The  $\Delta\chi^2$  has been computed using data for  $\sigma_{\text{polarized}}$ ,  $A_{\text{unpolarized}}$  and  $A_{\text{polarized}}$ ;  $\sigma_{\text{unpolarized}}$  was not included. A mass splitting of  $\Delta m_{\tilde{\chi}} = 200$  MeV was used in generating the pion momenta.

reviewed in the previous section. While some of the theoretical uncertainties in the widths cancel when computing the branching ratios, the latter will still have dependence on the  $M_1, M_2, \mu, \tan\beta$  parameters at the (2 – 5)% level for  $\Delta m_{\tilde{\chi}} \lesssim 700$  MeV (much larger as the multi-pion decay modes of the  $\tilde{\chi}_1^\pm$  enter at

$L=2\text{ab}^{-1}$  total,  $\sqrt{s}=600$  only,  $\sigma_{\text{unpol.}}$  excluded

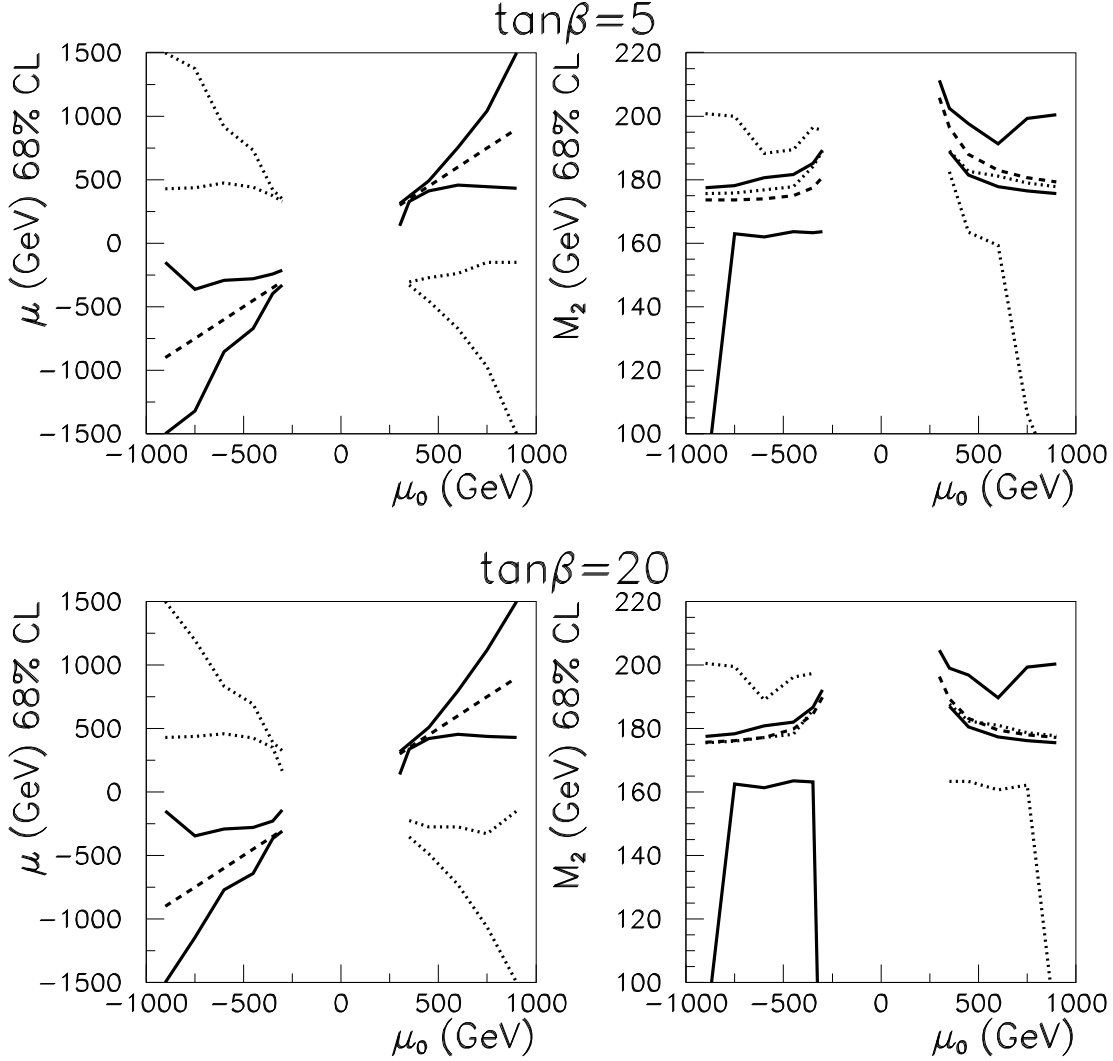


Figure 13: For  $m_{\tilde{\chi}_1^\pm} = 175$  GeV, we plot the upper and lower  $\Delta\chi^2 = 2.3$  (68% CL) limits for  $\mu$  and  $M_2$  as a function of the input value of  $\mu$ ,  $\mu_0$ , for input values of  $\tan\beta = 5$  and  $\tan\beta = 20$ . The dashed lines indicate either the input values of  $\mu_0$  or the corresponding  $M_2(\mu_0)$  values for the input  $\tan\beta$ , given  $m_{\tilde{\chi}_1^\pm} = 175$  GeV. For each  $\mu_0$ , the 68% CL boundaries for choices of  $\mu$  with the same (opposite) sign of  $\mu$  are shown by solid (dotted) lines. Points not plotted at small  $\mu \sim 300$  GeV are inconsistent with the given input  $m_{\tilde{\chi}_1^\pm} = 175$  GeV. Data inputs are as specified in Fig. 12.

somewhat larger  $\Delta m_{\tilde{\chi}}$ ). For this paper, we have assumed that the absolute normalization of the unpolarized absolute cross section is not computable to the 5% level, and have determined the  $\Delta\chi^2$  values using only  $A_{\text{unpolarized}}$ ,  $\sigma_{\text{polarized}}$  and  $A_{\text{polarized}}$ . If we were able to reliably use  $\sigma_{\text{unpolarized}}$ , the resulting plots analogous

to Fig. 12 would show a moderate increase in our ability to determine  $M_2$  and  $\mu$ , but  $\tan\beta$  would remain essentially undetermined.

We have also examined whether it is useful to include data from several  $\sqrt{s}$  choices for determining  $\mu, M_2, \tan\beta$ . We found that splitting the total luminosity between  $\sqrt{s} = 450$  GeV and 600 GeV actually causes a mild decrease in our ability to determine the parameters (assuming no large variation of instantaneous luminosity with  $\sqrt{s}$ ). This remains true even if we run at both energies and use as an observable the ratio  $\sigma_{\text{unpolarized}}(\sqrt{s} = 450 \text{ GeV})/\sigma_{\text{unpolarized}}(\sqrt{s} = 600 \text{ GeV})$  (which would be less affected by systematic theoretical uncertainties as compared to the individual absolute  $\sigma_{\text{unpolarized}}$  normalizations). If we are conservative and rely only on polarized data ( $L = 2 \text{ ab}^{-1}$  at  $\sqrt{s} = 600 \text{ GeV}$ ), the  $M_2$  and  $\mu$  accuracies are almost the same as shown in Fig. 12.

Additional information can, in principal, be gleaned from the  $\tilde{\chi}_1^\pm \rightarrow \tilde{\chi}_1^0 \pi^\pm$  decays. However, this is quite difficult in practice. The issue is whether one can use correlations involving the pions in the final state. Correlations between the pions themselves or between the pions and the reconstructed momenta for the  $\tilde{\chi}_1^\pm$  will be present to the extent that information regarding the direction of the spins  $s^\pm$  of the decaying  $\tilde{\chi}_1^\pm$  influences the  $\pi^\pm$ . Consider  $\tilde{\chi}_1^-$  decay. For a given  $s^-$  choice, one finds

$$|\mathcal{M}(\tilde{\chi}_1^- \rightarrow \pi^- \tilde{\chi}_1^0)|^2 \propto 1 + \frac{\Delta m_{\tilde{\chi}} - p_{\pi^-} \cdot s^-}{m_{\tilde{\chi}_1^\pm}} \quad (16)$$

after dropping terms higher order in the small ratios  $\Delta m_{\tilde{\chi}}/m_{\tilde{\chi}_1^\pm}$  and  $p_{\pi^-}/m_{\tilde{\chi}_1^\pm}$ . Since  $|\vec{p}_{\pi^-}|$  is of order  $\Delta m_{\tilde{\chi}}$ , the dependence on  $p_{\pi^-} \cdot s^-$  is obscured by the much larger leading term. For this reason, we have not attempted to employ these correlations.

**6. Discussion and Conclusions.** We have considered the detection at a linear  $e^+e^-$  collider of the lightest chargino in a model in which it is closely degenerate with a wino-like neutralino. The phenomenology depends critically upon the mass splitting  $\Delta m_{\tilde{\chi}} \equiv m_{\tilde{\chi}_1^\pm} - m_{\tilde{\chi}_1^0}$ . For  $\Delta m_{\tilde{\chi}} < m_\pi$ , one will observe long-lived heavily ionizing  $\tilde{\chi}_1^\pm$  tracks. For  $\Delta m_{\tilde{\chi}} \gtrsim 2 \text{ GeV}$ , the usual mSUGRA jets + missing energy signal will be dominant. Both can be detected for  $m_{\tilde{\chi}_1^\pm}$  essentially all the way up to the threshold at  $\sqrt{s}/2$  assuming modest integrated luminosity of  $L = 50 \text{ fb}^{-1}$ . For  $m_{\tilde{\chi}_1^\pm}$  not near threshold, much less luminosity would be adequate. For the range  $200 \text{ MeV} < \Delta m_{\tilde{\chi}} < 1 \text{ GeV}$ , favored in typical models, the  $\gamma + \pi^+\pi^- + \cancel{E}$  final state will be the crucial discovery mode. Then, so long as soft  $\gtrsim 200 \text{ MeV}$  pions are visible in the detector,<sup>7</sup> discovery in the  $\gamma + \pi^+\pi^- + \cancel{E}$  mode will be possible up to  $m_{\tilde{\chi}_1^\pm} \sim (\sqrt{s} - p_T^\gamma)/2$  for  $L = 50 \text{ fb}^{-1}$ . In particular, we argued that simple cuts requiring  $p_T^\gamma > 10 \text{ GeV}$ , only two soft/central pions, large (mainly invisible) mass recoiling opposite the trigger  $\gamma$ , and no small angle ( $\theta > 1^\circ$ )  $e^-$  or  $e^+$  (as would be present for the most obvious two-photon backgrounds) have an excellent chance of suppressing backgrounds to a negligible level. An overview of the discovery modes relevant as a function of location in the full  $[m_{\tilde{\chi}_1^\pm}, \Delta m_{\tilde{\chi}}]$  parameter space appeared in Fig. 2.

We then turned to a more detailed study of scenarios that would arise in the  $\delta_{GS} = 0$  O-II string model

<sup>7</sup>If the soft pions are not visible,  $\gamma \tilde{\chi}_1^+ \tilde{\chi}_1^-$  production yields a  $\gamma + \cancel{E}$  final state with substantial background from  $\gamma + Z(\rightarrow \nu\bar{\nu})$ , and discovery reach will be more limited and the error for  $m_{\tilde{\chi}_1^\pm}$ , summarized shortly, much larger;  $\Delta m_{\tilde{\chi}}$  will not be measurable.

and in the AMSB model. These models predict the same low-energy ratios for the gaugino masses,  $M_2 : M_1 : M_3 \sim 0.3 : 1 : 3$  (tree-level), and generally require substantial  $|\mu|$  for automatic electroweak symmetry breaking. In these models, the smallness of  $M_2$  compared to the other mass parameters implies that  $\Delta m_{\tilde{\chi}}$  will almost certainly lie in the  $m_\pi < \Delta m_{\tilde{\chi}} < 800$  MeV range (after including radiative corrections) for which the only appropriate mode for discovery and study is  $e^+e^- \rightarrow \gamma \tilde{\chi}_1^+ \tilde{\chi}_1^- \rightarrow \gamma \pi^+ \pi^- \tilde{\chi}_1^0 \tilde{\chi}_1^0$ . The large ratio of  $M_3/M_2$  implies that fine tuning for these models will be quite extreme unless the chargino mass lies in the  $< 200$  GeV range. For  $m_{\tilde{\chi}_1^\pm}$  and  $\Delta m_{\tilde{\chi}}$  in these ranges we studied the accuracy with which  $m_{\tilde{\chi}_1^\pm}$  and  $\Delta m_{\tilde{\chi}}$  can be measured using kinematic distributions of the pions in the final state. For the particularly typical choices of  $m_{\tilde{\chi}_1^\pm} = 175$  GeV and  $\Delta m_{\tilde{\chi}} = 200$  MeV, we studied the accuracy with which the  $\Delta m_{\tilde{\chi}}$  and  $c\tau$  could be determined from the transverse impact parameter distribution for the soft pion tracks. Finally, for  $m_{\tilde{\chi}_1^\pm} = 175$  GeV and  $\Delta m_{\tilde{\chi}} = 200$  MeV, we determined the precision with which the fundamental underlying SUSY parameters  $M_2$ ,  $\mu$  and  $\tan\beta$  could be determined from cross sections and asymmetries. We summarize the results of these studies below.

The errors estimated for  $m_{\tilde{\chi}_1^\pm}$  and  $\Delta m_{\tilde{\chi}}$  assume that the electron sneutrino is not so light as to substantially suppress the unpolarized  $\gamma \tilde{\chi}_1^+ \tilde{\chi}_1^-$  cross section. Error estimates for  $m_{\tilde{\chi}_1^\pm}$  and  $\Delta m_{\tilde{\chi}}$  obtained by studying kinematic distributions of the final pion decay products were given for two procedures, assuming  $L = 1$  ab $^{-1}$  of accumulated data. The first employs events in which the  $\tilde{\chi}_1^+ \tilde{\chi}_1^-$  invariant mass is very close to  $2m_{\tilde{\chi}_1^\pm}$  (i.e. events with very large  $p_T^\gamma$ ). After accumulating  $L = 1$  ab $^{-1}$  with unpolarized beams, we find that the location of the threshold for the recoil mass opposite the  $\gamma$  trigger (i.e. the invariant mass of the  $\tilde{\chi}_1^+ \tilde{\chi}_1^-$  pair system), denoted  $M_{\chi\chi}$ , gives a very accurate measurement of  $m_{\tilde{\chi}_1^\pm}$  (typically  $< 0.5\%$  error), and that the average soft  $\pi$  energy,  $E_\pi^*$ , in the  $M_{\chi\chi}$  center of mass for  $M_{\chi\chi}$  near threshold gives a very accurate measurement of  $\Delta m_{\tilde{\chi}}$  (typically 1%). These procedures for detecting  $\gamma \tilde{\chi}_1^+ \tilde{\chi}_1^-$  and measuring  $m_{\tilde{\chi}_1^\pm}$  and  $\Delta m_{\tilde{\chi}}$  using only events with the highest photon energies, such that  $M_{\chi\chi} \sim 2m_{\tilde{\chi}_1^\pm}$ , guarantee that these goals can be achieved even if there is significant background (contrary to our expectation) at lower  $E_\gamma$  and  $p_T^\gamma$  for the photon tag. Only if  $m_{\tilde{\chi}_1^\pm}$  is close to  $\sqrt{s}/2$  would we have to rely on the background being small for  $p_T^\gamma$  as small as 10 GeV. However, if we are correct that this background remains small for such a low  $p_T^\gamma$  for the trigger, slightly better accuracies for  $m_{\tilde{\chi}_1^\pm}$  and  $\Delta m_{\tilde{\chi}}$  can be achieved (for all, but especially moderate,  $m_{\tilde{\chi}_1^\pm}$  values) by employing the full  $[E_\pi^*, M_{\chi\chi}]$  distribution of the events and applying statistical tests for discriminating between the distributions obtained for different  $[m_{\tilde{\chi}_1^\pm}, \Delta m_{\tilde{\chi}}]$  choices. We emphasize that the low  $p_T^\gamma$  events will *certainly* be background free if  $\Delta m_{\tilde{\chi}} \lesssim 600$  MeV (as typical) since in almost all events one or both of the final  $\pi$ 's will have an observable high impact parameter (HIP).

For the typical case of  $m_{\tilde{\chi}_1^\pm} = 175$  GeV and  $\Delta m_{\tilde{\chi}} = 200$  MeV (for which essentially all events have a HIP  $\pi$  and, hence, backgrounds are certain to be small even when including all events with  $p_T^\gamma > 10$  GeV), we found that for  $L = 1$  ab $^{-1}$  the value of  $\Delta m_{\tilde{\chi}}$  can be determined to better than 1 MeV from the transverse impact parameter distribution of the final pions. Simultaneously,  $c\tau$  for the  $\tilde{\chi}_1^\pm \rightarrow \pi^\pm \tilde{\chi}_1^0$  decay can be determined to roughly 2%. (The impact distribution is less sensitive to  $m_{\tilde{\chi}_1^\pm}$ , which is best determined from the kinematic distributions.)



Finally, the underlying parameters  $M_2$  and  $\mu$  of supersymmetry can be most reliably determined from the magnitude of the  $\gamma\tilde{\chi}_1^+\tilde{\chi}_1^-$  right-handed polarized  $e^-$  beam cross section and the polarized beam and unpolarized beam angular asymmetries. As part of the procedure, one inputs the precise determination of  $m_{\tilde{\chi}_1^\pm}$  obtained by employing the threshold or statistical techniques. For the typical  $m_{\tilde{\chi}_1^\pm} = 175$  GeV,  $\Delta m_{\tilde{\chi}} = 200$  MeV case, we determined the statistical errors for these quantities assuming  $L = 1$  ab $^{-1}$  each in unpolarized and polarized running. We then computed the  $\Delta\chi^2$  for discriminating between a given input model choice of  $M_2, \mu, \tan\beta$  (constrained to give the value of  $m_{\tilde{\chi}_1^\pm} = 175$  GeV, presumed to already be well-measured) and other possible choices consistent with the same  $m_{\tilde{\chi}_1^\pm}$  value.<sup>8</sup> We found the best parameter accuracies by accumulating luminosity only at the highest energy ( $\sqrt{s} = 600$  GeV in our study), distributed roughly equally between unpolarized beam running and pure  $e_R^-$  running. We found  $1\sigma$  (68% CL) accuracies for  $M_2$  and  $|\mu|$  of  $\pm 8\%$  and  $\pm 16\%$ , respectively, for  $|\mu| \sim 400$  GeV, and  $\pm 8\%$  and  $\pm 40\%$ , respectively, for  $|\mu| \sim 600$  GeV. Errors for both  $M_2$  and  $|\mu|$  become uselessly large by  $|\mu| \sim 900$  GeV. The sign of  $\mu$  is not determined at the  $1\sigma$  level. However, the error for  $M_2$  decreases to about 5% for  $350 \text{ GeV} < |\mu| < 750 \text{ GeV}$  if the sign of  $\mu$  is known from other input. Finally,  $\tan\beta$  is essentially undetermined at the  $1\sigma$  level. We have noted that for the small values of  $\Delta m_{\tilde{\chi}}$  natural in the wino LSP scenarios, correlations involving the final soft  $\pi$ 's are negligible and do not aid in parameter determination.

In the above, we did not employ the absolute normalization of the unpolarized cross section since it is sensitive to many theoretical uncertainties at the (5 – 10)% level, a level of uncertainty that is larger than the amount of variation with respect to the parameters of interest. One source of uncertainty is the unknown  $\tilde{\nu}_e$  mass. By measuring the unpolarized  $\gamma\tilde{\chi}_1^+\tilde{\chi}_1^-$  cross section at two energies,  $m_{\tilde{\nu}_e}$  could be extracted with an accuracy determined by the other theoretical uncertainties in  $\sigma_{\text{unpolarized}}$ . However, if we expend luminosity for this purpose, the errors for the  $M_2$  and  $\mu$  determinations would increase.

Of course, additional SUSY signals *will* emerge if some of the squarks, sleptons and/or sneutrinos are light enough (but still heavier than the  $\tilde{\chi}_1^\pm$ ) that their production rates are substantial. In particular, leptonic signals from the decays [*e.g.*  $\tilde{\ell}_L^\pm \rightarrow \ell^\pm\tilde{\chi}_1^0$  or  $\tilde{\nu}_\ell \rightarrow \ell^\pm\tilde{\chi}_1^\mp$ ] would be present. Also, depending upon  $\sqrt{s}$  and the mass splitting between the wino-like  $\tilde{\chi}_1^0$  and the bino-like  $\tilde{\chi}_2^0$  (which is large in many models), the suppressed  $\tilde{\chi}_1^0\tilde{\chi}_2^0$  production channel might be detectable. Or, the radiative electroweak symmetry breaking scenario chosen by nature could be sufficiently unconventional that  $|\mu|$  is small enough for production of charged and neutral higgsino-like states to be detectable. We have chosen to emphasize the case (which is most likely in typical models) that none of these additional signals are present until  $\sqrt{s}$  substantially above 600 GeV is available.

It is, of course, likely that the LHC will have been operating for a number of years prior to the construction of the next  $e^+e^-$  collider. Because of the large available center of mass energy, it is probable that some of the heavier states mentioned above will be produced. However, it is not completely clear that they will be observed. The role of the LHC for the type of model being considered will be discussed in a

---

<sup>8</sup>Values of  $|\mu| < 300$  GeV were not considered; for such values,  $\tilde{\chi}_2^\pm$  production becomes possible and the strategy for determining SUSY parameters would change substantially.

later paper.

### Acknowledgements

This work was supported by the Department of Energy and by the Davis Institute for High Energy Physics. JFG would like to acknowledge the hospitality of the Aspen Center for Physics during a portion of this work.

### 7. Appendix

In this Appendix we present some details regarding the reconstruction of the momenta of all the particles for the process  $e^+e^- \rightarrow \gamma\tilde{\chi}_1^+\tilde{\chi}_1^- \rightarrow \gamma\pi^+\tilde{\chi}_1^0\pi^-\tilde{\chi}_1^0$ . (We use the notation  $\tilde{\chi}_1^0$  to distinguish the  $\tilde{\chi}_1^0$  associated with the  $\tilde{\chi}_1^+$  decay; the  $\tilde{\chi}_1^0$  is, of course, its own antiparticle.) We also give the form of the  $\gamma\tilde{\chi}_1^+\tilde{\chi}_1^-$  cross section resulting from the often dominant terms (a gauge invariant subset) in which the  $\gamma$  is radiated only from an initial  $e^+$  or  $e^-$ .

The reconstruction of the final state momenta is performed in analogy with the techniques developed for  $e^+e^- \rightarrow W^+W^- \rightarrow \ell^+\nu\ell^-\bar{\nu}$  [24]. We begin by first using the observed  $\gamma$  four momentum and the known  $e^+$  and  $e^-$  beam momenta to boost to the  $\tilde{\chi}_1^+\tilde{\chi}_1^-$  center of mass. The momenta in the expressions below are those defined in this frame. (We drop the \* superscripts employed in the main text.) In the  $\tilde{\chi}_1^+\tilde{\chi}_1^-$  c.m.s., the 6 components of the observed  $\pi^+$  and  $\pi^-$  three momenta, combined with the known  $m_{\tilde{\chi}_1^0}$  and  $m_{\tilde{\chi}_1^\pm}$  masses, can be used to solve for the three momenta of the  $\tilde{\chi}_1^0$  and  $\tilde{\chi}_1^0$  up to a two-fold ambiguity indicated by the  $\pm d$  term below:

$$\vec{p}_{\tilde{\chi}_1^0} = a\vec{p}_{\pi^-} + b\vec{p}_{\pi^+} \pm d(\vec{p}_{\pi^-} \times \vec{p}_{\pi^+}), \quad \vec{p}_{\tilde{\chi}_1^0} = -(\vec{p}_{\tilde{\chi}_1^0} + \vec{p}_{\pi^+} + \vec{p}_{\pi^-}), \quad (17)$$

where  $a$ ,  $b$  and  $d$  are given by:<sup>9</sup>

$$a = \frac{m|\vec{p}_{\pi^+}|^2 - n\vec{p}_{\pi^-} \cdot \vec{p}_{\pi^+}}{|\vec{p}_{\pi^-} \times \vec{p}_{\pi^+}|^2}, \quad b = \frac{-m\vec{p}_{\pi^-} \cdot \vec{p}_{\pi^+} + n|\vec{p}_{\pi^-}|^2}{|\vec{p}_{\pi^-} \times \vec{p}_{\pi^+}|^2},$$

$$d^2 = \frac{(E_b - E_{\pi^-})^2 - m_{\tilde{\chi}_1^0}^2 - a^2|\vec{p}_{\pi^-}|^2 - b^2|\vec{p}_{\pi^+}|^2 - 2ab\vec{p}_{\pi^-} \cdot \vec{p}_{\pi^+}}{|\vec{p}_{\pi^-} \times \vec{p}_{\pi^+}|^2}, \quad (18)$$

where

$$m \equiv -\frac{1}{2} \left( m_{\tilde{\chi}_1^\pm}^2 - m_{\tilde{\chi}_1^0}^2 - 2E_b E_{\pi^-} + E_{\pi^-}^2 + |\vec{p}_{\pi^-}|^2 \right), \quad n \equiv \frac{1}{2} \left( m_{\tilde{\chi}_1^\pm}^2 - m_{\tilde{\chi}_1^0}^2 - 2E_b E_{\pi^+} - 2\vec{p}_{\pi^-} \cdot \vec{p}_{\pi^+} \right). \quad (19)$$

Using these formulae, we can, up to the two-fold ambiguity, reconstruct the  $\tilde{\chi}_1^+$  and  $\tilde{\chi}_1^-$  momenta. The construction only fails if  $\vec{p}_{\pi^-} \times \vec{p}_{\pi^+} = 0$  or if  $d^2 < 0$  (the latter being possible as a result of momentum smearing in the detector). If  $d^2 < 0$ , setting  $d = 0$  usually gives a fairly accurate result for  $\vec{p}_{\tilde{\chi}_1^0}$  and  $\vec{p}_{\tilde{\chi}_1^0}$ . It is perhaps useful to keep in mind approximations that follow from the fact that  $E_{\pi^+}, E_{\pi^-}, |\vec{p}_{\pi^+}|, |\vec{p}_{\pi^-}| \sim \Delta m_{\tilde{\chi}}$  and  $m_{\tilde{\chi}_1^\pm}^2 - m_{\tilde{\chi}_1^0}^2 \sim 2m_{\tilde{\chi}_1^0}\Delta m_{\tilde{\chi}}$ . For small  $\Delta m_{\tilde{\chi}}/m_{\tilde{\chi}_1^0}$  we have

$$m = E_b E_{\pi^-} - m_{\tilde{\chi}_1^0}\Delta m_{\tilde{\chi}}, \quad n = -E_b E_{\pi^+} + m_{\tilde{\chi}_1^0}\Delta m_{\tilde{\chi}}, \quad d = \frac{\sqrt{E_b^2 - m_{\tilde{\chi}_1^0}^2}}{|\vec{p}_{\pi^-} \times \vec{p}_{\pi^+}|}. \quad (20)$$

<sup>9</sup>We correct some errors in the formulae of Ref. [24].

Further,  $\vec{p}_{\tilde{\chi}_1^+} = \vec{p}_{\tilde{\chi}_1^0} + \vec{p}_{\pi^-} \sim \vec{p}_{\tilde{\chi}_1^0}$  and  $\vec{p}_{\tilde{\chi}_1^-} = \vec{p}_{\tilde{\chi}_1^0} + \vec{p}_{\pi^+} \sim \vec{p}_{\tilde{\chi}_1^0}$ . Finally, we note that if  $E_b > m_{\tilde{\chi}_1^\pm} \Delta m_{\tilde{\chi}}/m_\pi$ , the  $\pi$  directions are guaranteed to have positive dot product with the directions of their parent charginos.

The utility of this reconstruction follows from an understanding of how the matrix element squared depends upon the final state momenta. As described in the text, correlations between the helicity of the  $\tilde{\chi}_1^\pm$  and the three-momentum of the decay pion are of order  $\Delta m_{\tilde{\chi}}/m_{\tilde{\chi}_1^\pm}$ . Thus, to a very good approximation the distribution of the decay pion in the  $\tilde{\chi}_1^\pm$  rest frame is completely independent of the  $\theta^*, \phi^*$  rest frame decay angles for any fixed helicity of the  $\tilde{\chi}_1^\pm$ . The final state only contains information encoded in the decay distributions of the  $\tilde{\chi}_1^+, \tilde{\chi}_1^-$ . Thus, aside from small terms of order  $\Delta m_{\tilde{\chi}}/m_{\tilde{\chi}_1^\pm}$ , the decay pions do not have any correlations other than those kinematically induced by the boosts in the directions of their parent charginos and the form of the cross section as a function of  $\theta$ , the angle of the  $\tilde{\chi}_1^-$  in the  $\tilde{\chi}_1^+ - \tilde{\chi}_1^-$  center-of-mass.

For the case of a photon radiated from the initial  $e^+$  or  $e^-$ , the form of the invariant matrix element squared for  $e^+e^- \rightarrow \gamma \tilde{\chi}_1^+ \tilde{\chi}_1^-$  is  $|\mathcal{A}|^2 = (2p_{e^+} \cdot p_\gamma p_{e^-} \cdot p_\gamma)^{-1} |\mathcal{B}|^2$  with

$$\begin{aligned}
|\mathcal{B}|^2 \propto & -2\vec{p}_{\tilde{\chi}_1^-} \cdot p_{e^-} \vec{p}_{\tilde{\chi}_1^+} \cdot p_{e^+} p_{e^+} \cdot p_\gamma (Q_{LL}^2 + Q_{LR}^2 + Q_{RL}^2 + Q_{RR}^2) \\
& -2\vec{p}_{\tilde{\chi}_1^-} \cdot p_{e^-} \vec{p}_{\tilde{\chi}_1^+} \cdot p_{e^+} s (Q_{LR}^2 + Q_{RL}^2) \\
& +2\vec{p}_{\tilde{\chi}_1^-} \cdot p_{e^-} \vec{p}_{\tilde{\chi}_1^+} \cdot p_{e^+} (p_{e^-} \cdot p_\gamma Q_{LR}^2 + p_{e^-} \cdot p_\gamma Q_{RL}^2 + p_{e^+} \cdot p_\gamma Q_{LR}^2 + p_{e^+} \cdot p_\gamma Q_{RL}^2) \\
& +\vec{p}_{\tilde{\chi}_1^-} \cdot p_{e^-} s \vec{p}_{\tilde{\chi}_1^+} \cdot p_\gamma (Q_{LR}^2 + Q_{RL}^2) \\
& -2\vec{p}_{\tilde{\chi}_1^-} \cdot p_{e^-} \vec{p}_{\tilde{\chi}_1^+} \cdot p_\gamma p_{e^-} \cdot p_\gamma (Q_{LR}^2 + Q_{RL}^2) \\
& -2\vec{p}_{\tilde{\chi}_1^-} \cdot p_{e^+} \vec{p}_{\tilde{\chi}_1^+} \cdot p_{e^-} s (Q_{LL}^2 + Q_{RR}^2) \\
& +2\vec{p}_{\tilde{\chi}_1^-} \cdot p_{e^+} \vec{p}_{\tilde{\chi}_1^+} \cdot p_{e^-} (p_{e^-} \cdot p_\gamma Q_{LL}^2 + p_{e^-} \cdot p_\gamma Q_{RR}^2 + p_{e^+} \cdot p_\gamma Q_{LL}^2 + p_{e^+} \cdot p_\gamma Q_{RR}^2) \\
& -2\vec{p}_{\tilde{\chi}_1^-} \cdot p_{e^+} \vec{p}_{\tilde{\chi}_1^+} \cdot p_{e^+} p_{e^-} \cdot p_\gamma (Q_{LL}^2 + Q_{LR}^2 + Q_{RL}^2 + Q_{RR}^2) \\
& +\vec{p}_{\tilde{\chi}_1^-} \cdot p_{e^+} s \vec{p}_{\tilde{\chi}_1^+} \cdot p_\gamma (Q_{LL}^2 + Q_{RR}^2) \\
& -2\vec{p}_{\tilde{\chi}_1^-} \cdot p_{e^+} \vec{p}_{\tilde{\chi}_1^+} \cdot p_\gamma p_{e^+} \cdot p_\gamma (Q_{LL}^2 + Q_{RR}^2) \\
& +\vec{p}_{\tilde{\chi}_1^+} \cdot p_{e^-} s \vec{p}_{\tilde{\chi}_1^-} \cdot p_\gamma (Q_{LL}^2 + Q_{RR}^2) \\
& -2\vec{p}_{\tilde{\chi}_1^+} \cdot p_{e^-} \vec{p}_{\tilde{\chi}_1^-} \cdot p_\gamma p_{e^-} \cdot p_\gamma (Q_{LL}^2 + Q_{RR}^2) \\
& +\vec{p}_{\tilde{\chi}_1^+} \cdot p_{e^+} s \vec{p}_{\tilde{\chi}_1^-} \cdot p_\gamma (Q_{LR}^2 + Q_{RL}^2) \\
& -2\vec{p}_{\tilde{\chi}_1^+} \cdot p_{e^+} \vec{p}_{\tilde{\chi}_1^-} \cdot p_\gamma p_{e^+} \cdot p_\gamma (Q_{LR}^2 + Q_{RL}^2) \\
& -s^2 m_{\tilde{\chi}_1^\pm}^2 (Q_{LL} Q_{LR} + Q_{RL} Q_{RR}) \\
& +2s m_{\tilde{\chi}_1^\pm}^2 (p_{e^-} \cdot p_\gamma Q_{LL} Q_{LR} + p_{e^-} \cdot p_\gamma Q_{RL} Q_{RR} + p_{e^+} \cdot p_\gamma Q_{LL} Q_{LR} + p_{e^+} \cdot p_\gamma Q_{RL} Q_{RR}) \\
& -2m_{\tilde{\chi}_1^\pm}^2 ((p_{e^-} \cdot p_\gamma)^2 Q_{LL} Q_{LR} + (p_{e^-} \cdot p_\gamma)^2 Q_{RL} Q_{RR} + (p_{e^+} \cdot p_\gamma)^2 Q_{LL} Q_{LR} + (p_{e^+} \cdot p_\gamma)^2 Q_{RL} Q_{RR}).
\end{aligned}$$

In the above, all  $Q_{\alpha\beta}$ 's are evaluated at  $M_{\tilde{\chi}\tilde{\chi}}^2$ . Note that  $|\mathcal{A}|^2$  reduces to Eq. (13) in the  $p_\gamma \rightarrow 0$  limit after removing the photon radiation pole factors  $(p_{e^+} \cdot p_\gamma)(p_{e^-} \cdot p_\gamma)$ . This answer is gauge invariant on its own. Contributions to  $|\mathcal{A}|^2$  coming from diagrams in which the photon is radiated from one of the final  $\tilde{\chi}_1^\pm$  lines are often suppressed relative to the initial state radiation terms given above. All diagrams were included in our numerical calculations. In practice, there are delicate cancellations between large terms in Eq. (21), and also in the full expression for  $|\mathcal{A}|^2$  obtained after including all diagrams, that can lead to numerical inaccuracies. Thus, it is actually best to sum all the diagrams numerically at the matrix element level and

then square. This is the approach used in our numerical simulations.

## References

- [1] A. Brignole, L.E. Ibanez, and C. Munoz, Nucl. Phys. **B422** (1994) 125, Erratum, *ibid.*, **B436** (1995) 747; hep-ph/9707209.
- [2] C.H. Chen, M. Drees, and J.F. Gunion, Phys. Rev. Lett. **76** (1996) 2002 [Erratum-*ibid.* **82**, 3192 (1999)] .
- [3] C. H. Chen, M. Drees and J. F. Gunion, Phys. Rev. D **55**, 330 (1997) [Erratum-*ibid.* D **60**, 039901 (1999)] [hep-ph/9607421].
- [4] C.H. Chen, M. Drees, and J.F. Gunion, hep-ph/9902309.
- [5] L. Randall and R. Sundrum, Nucl. Phys. **B557**, 79 (1999) [hep-th/9810155].
- [6] G. F. Giudice, M. A. Luty, H. Murayama and R. Rattazzi, JHEP **9812**, 027 (1998) [hep-ph/9810442].
- [7] A. Pomarol and R. Rattazzi, JHEP **9905**, 013 (1999) [hep-ph/9903448].
- [8] G. Anderson, C.H. Chen, J.F. Gunion, J. Lykken, T. Moroi and Y. Yamada, hep-ph/9609457, published in *New Directions for High Energy Physics*, Proceedings of the Snowmass96 Summer Study, June 25 – July 12, 1996, Snowmass CO, eds. D.G. Cassel, L.T. Gennari, and R.H. Siemann, p. 669.
- [9] T. Gherghetta, G. F. Giudice and J. D. Wells, Nucl. Phys. **B559**, 27 (1999) [hep-ph/9904378].
- [10] J. L. Feng, T. Moroi, L. Randall, M. Strassler and S. Su, Phys. Rev. Lett. **83**, 1731 (1999).
- [11] J. F. Gunion and S. Mrenna, Phys. Rev. **D62**, 015002 (2000).
- [12] F. E. Paige and J. Wells, hep-ph/0001249.
- [13] S. Mizuta, D. Ng, and M. Yamaguchi, Phys. Lett. **B300** (1993) 96. A. Papadopoulos and D. Pierce, Nucl. Phys. **B430** (1994) 278. D. Pierce, J. Bagger, K. Matchev, and R.-J. Zhang, Nucl. Phys. **B491** (1997) 3.
- [14] H. Cheng, B. A. Dobrescu and K. T. Matchev, Nucl. Phys. B **543**, 47 (1999) [hep-ph/9811316].
- [15] A. Datta and S. Maity, Phys. Rev. D **59**, 055019 (1999) [hep-ph/9808423].
- [16] M. Bastero-Gil, G. L. Kane and S. F. King, Phys. Lett. **B474**, 103 (2000) [hep-ph/9910506].
- [17] G. Landsberg (DØ Collaboration), private communication; D. Cutts and G. Landsberg, hep-ph/9904396.

- [18] P. Abreu *et al.* [DELPHI Collaboration], Eur. Phys. J. **C11**, 1 (1999) [hep-ex/9903071] and CERN-EP-2000-033.
- [19] M. Acciarri *et al.* [L3 Collaboration], Phys. Lett. **B482**, 31 (2000) [hep-ex/0002043].
- [20] We employ the 1D and 2D KS tests as detailed in *Numerical Recipes*, W.H. Press *et al.*, Cambridge University Press, p. 617 (1D) and p. 640 (2D).
- [21] J.F. Gunion and H. Haber, Phys. Rev. **D37** (1988) 2515.
- [22] S. Y. Choi, A. Djouadi, M. Guchait, J. Kalinowski, H. S. Song and P. M. Zerwas, Eur. Phys. J. **C14**, 535 (2000) [hep-ph/0002033]; S. Y. Choi, A. Djouadi, H. Dreiner, J. Kalinowski and P. M. Zerwas, Eur. Phys. J. **C7**, 123 (1999) [hep-ph/9806279].
- [23] J.C. Collins and D. Soper, Phys. Rev. **D16** (1977) 2219.
- [24] D. Charlton, OPAL Technical Note TN536. Aside from changes necessitated by  $m_\pi \neq 0$  and  $m_{\tilde{\chi}_1^0} \neq 0$ , several typos and one inadvertent error in the Appendix of this paper are corrected.